Cell Reports
Article

Expanded Coverage of the 26S Proteasome Conformational Landscape Reveals Mechanisms of Peptidase Gating

Markus R. Eisele,[1,4] Randi G. Reed,[2,4] Till Rudack,[3,4] Andreas Schweitzer,[1,5] Florian Beck,[1,5] Istvan Nagy,[1] Günter Pfeifer,[1] Jürgen M. Plitzko,[1] Wolfgang Baumeister,[1,*] Robert J. Tomko, Jr.,[2,6,*] and Eri Sakata[1,*]
[1]Department of Molecular Structural Biology, Max Planck Institute of Biochemistry, 82152 Martinsried, Germany
[2]Department of Biomedical Sciences, Florida State University College of Medicine, Tallahassee, FL 32306-4300, USA
[3]Department of Biophysics, Ruhr University Bochum, 44801 Bochum, Germany
[4]These authors contributed equally
[5]These authors contributed equally
[6]Lead Contact
*Correspondence: baumeist@biochem.mpg.de (W.B.), robert.tomko@med.fsu.edu (R.J.T.), sakata@biochem.mpg.de (E.S.)
https://doi.org/10.1016/j.celrep.2018.07.004

SUMMARY

The proteasome is the central protease for intracellular protein breakdown. Coordinated binding and hydrolysis of ATP by the six proteasomal ATPase subunits induces conformational changes that drive the unfolding and translocation of substrates into the proteolytic 20S core particle for degradation. Here, we combine genetic and biochemical approaches with cryo-electron microscopy and integrative modeling to dissect the relationship between individual nucleotide binding events and proteasome conformational dynamics. We demonstrate unique impacts of ATP binding by individual ATPases on the proteasome conformational distribution and report two conformational states of the proteasome suggestive of a rotary ATP hydrolysis mechanism. These structures, coupled with functional analyses, reveal key roles for the ATPases Rpt1 and Rpt6 in gating substrate entry into the core particle. This deepened knowledge of proteasome conformational dynamics reveals key elements of intersubunit communication within the proteasome and clarifies the regulation of substrate entry into the proteolytic chamber.

INTRODUCTION

The ubiquitin-proteasome system (UPS) conducts most regulated protein degradation in eukaryotes (Tomko and Hochstrasser, 2013) and is frequently deregulated in human disease (Schmidt and Finley, 2014). UPS substrates are typically first modified with chains of the small protein ubiquitin (polyUb), which targets the substrate to the 26S proteasome for degradation. The 26S proteasome is a 2.5 MDa multisubunit ATP-dependent peptidase complex that consists of a barrel-shaped proteolytic 20S core particle (CP) and one or two 19S regulatory particles (RPs) that cap the CP ends (Voges et al., 1999). The CP comprises four heptameric rings stacked upon a central axis in the order α_{1-7}-β_{1-7}-β_{1-7}-α_{1-7}. The β rings form a catalytic chamber with three different peptidase activities whereas the α rings control substrate entry into the proteolytic chamber via a gate formed by their N-terminal extensions (Baumeister et al., 1998; Groll et al., 2000).

The RP consists of two subcomplexes, the lid and base. The lid consists of nine RP non-ATPase (Rpn) subunits, Rpn3, Rpn5–Rpn9, Rpn11, Rpn12, and Rpn15/Sem1. Rpn11 contains a metallopeptidase activity that removes the polyUb targeting signal from the substrate. The base consists of three substrate receptors (Rpn1, Rpn10, and Rpn13) that bind incoming polyubiquitinated substrates and a hexameric ring of AAA+ family ATPases (Rpt1–Rpt6) that form a central channel (Finley et al., 2016). The ATPases are motor enzymes that use ATP-dependent motions of conserved aromatic-hydrophobic pore loops to grasp and pull the substrate for unfolding and translocation into the CP (Nyquist and Martin, 2014). In addition, they serve as activators of proteolysis by opening the CP gate to allow substrate entry (Smith et al., 2007). The C termini of most proteasome activators contain hydrophobic-tyrosine-X (HbYX) motifs, which insert into α-ring pockets to trigger gate opening (Rabl et al., 2008; Smith et al., 2007). Cryo-electron microscopy (cryo-EM) studies of the eukaryotic 26S proteasome revealed that the conserved HbYX motifs of Rpt2, Rpt3, and Rpt5 stably insert into the α-ring pockets but do not trigger gate-opening (Chen et al., 2016; Wehmer et al., 2017). Thus, the molecular mechanism of gating by the RP remains very poorly understood.

Cryo-EM studies of the 26S proteasome from our group (Guo et al., 2018; Lasker et al., 2012; Unverdorben et al., 2014; Wehmer et al., 2017) and others (Chen et al., 2016; Huang et al., 2016; Lander et al., 2012; Matyskiela et al., 2013) have revealed at least four distinct conformational states (herein called s1–s4) that appear conserved between yeast, rat, and human proteasomes (reviewed in Bard et al., 2018 and Wehmer and Sakata, 2016). The s1 state (similar to the apo [Lander et al., 2012], S_A [Chen et al., 2016], or M2 [Huang et al., 2016]) is likely inactive because the channels of the ATPase ring and CP are misaligned, and Rpn11 is located ~25 Å away from the ATPase pore with its

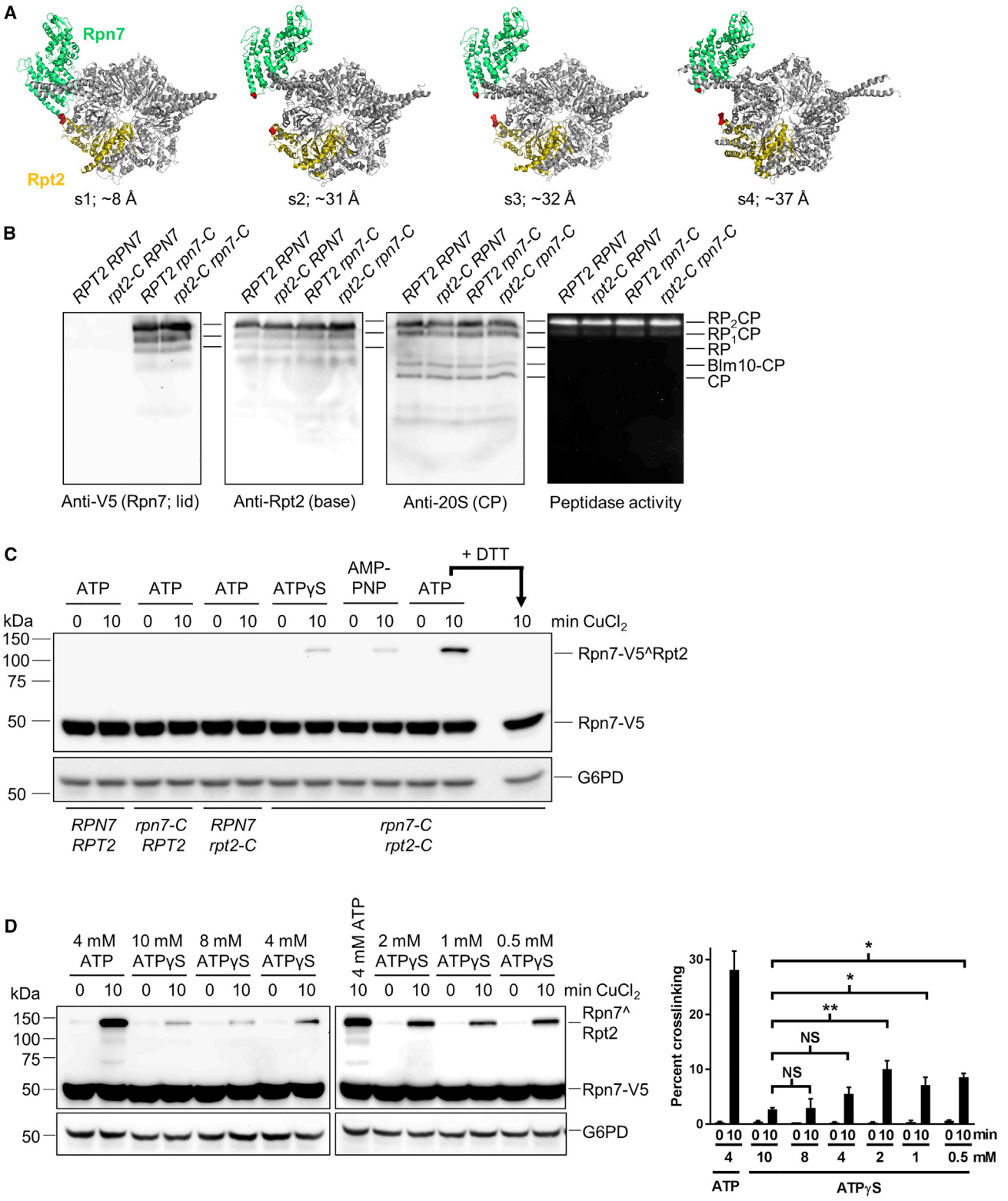

Figure 1. A Conformation-Selective Reporter of the Proteasome Reveals Nucleotide Concentration-Dependent State Switching

(A) Juxtaposition of Rpn7-D123 and Rpt2-R407 (red spheres) in the s1, s2, s3, and s4 states is shown with distances between α carbons listed. Rpn7, green; Rpt2, gold; the other five Rpt subunits, gray. Other subunits are omitted for clarity.

(legend continued on next page)

catalytic site inaccessible. In contrast, the s2–s4 states appear configured for substrate processing due to large-scale conformational reorganizations that align Rpn11 and the ATPase pore with the axial channel of the CP. Although the s2 (similar to the S_B state [Chen et al., 2016]) and s3 (similar to the substrate-bound [Matyskiela et al., 2013], S_C [Chen et al., 2016], or M1 states [Huang et al., 2016]) states are primed for substrate degradation, the CP gate is mostly occluded, preventing substrate entry. Our previous work (Wehmer et al., 2017) showed that the s4 state lacks density corresponding to the CP gate, suggesting that it represents a fully active proteasome. A similar state, S_D, was recently reported for human proteasomes purified in the presence of ATP (Chen et al., 2016). Due to the limited resolution of these EM maps, the nucleotide state of each ATPase could not be unambiguously determined. Thus, the relationship between individual nucleotide binding events, the proteasome conformational equilibrium, and CP gating remain unclear.

Using a combined genetic, biochemical, and structural approach, we dissect the impact of individual nucleotide binding events on the conformational equilibrium of the proteasome. Conformation-selective crosslinking and EM analyses of proteasomes impaired for ATP hydrolysis in individual ATPase subunits revealed distinct impacts on the conformational distribution and revealed two previously unreported conformational states of the proteasome, both of which display open gates. A unifying feature of the open-gate states is insertion of the Rpt1 and Rpt6 C termini into the α ring, and we demonstrate that the Rpt1 and Rpt6 tails cooperate to open the CP gate for proteolysis. Together, our work expands the known conformational landscape of the proteasome, provides novel insights into the ATPase cycle, and rationalizes previous studies demonstrating that stable docking of HbYX motifs into the CP is insufficient to promote peptidase gating.

RESULTS

A Conformation-Selective Reporter for the Proteasome

The conformation of the 26S proteasome has thus far been studied almost exclusively by time- and effort-intensive cryo-EM single particle analyses. Thus, we sought a simple biochemical reporter for proteasome conformational state that would permit rapid comparison of multiple experimental conditions. Guided by recent structures of the yeast proteasome in ground (s1) and activated (s2–s4) states (Wehmer et al., 2017), we identified amino acids that, when replaced with cysteines, would be close enough for disulfide bond formation in one state, but not the others. Addition of a mild oxidant, such as Cu^{2+}, would then promote conformation-selective crosslinks that could be visualized as a bandshift by non-reducing SDS-PAGE (Tomko et al., 2010). Although we were unable to identify residues that underwent sufficient distance changes to discriminate the s2, s3, and s4 states from one another, we identified several pairs that allowed discrimination of the s1 state from s2–s4. Specifically, the α carbon atom distance between Asp123 in the lid subunit Rpn7 and Arg407 of the base subunit Rpt2 in the s1 state is ~8 Å. In the s2–s4 states, the distance is >31 Å, precluding disulfide formation (Figure 1A).

We introduced *rpt2*(*R407C*) or *rpn7*(*D123C*)-*V5* alleles singly or jointly into the respective chromosomal loci in yeast. These substitutions had no apparent effect on cell growth under known proteasome stresses (Kusmierczyk et al., 2008) (Figure S1A) and cells harboring them had no apparent defects in proteasome assembly, abundance, or peptidase activity by native PAGE (Figure 1B). As a test for conformational selectivity, we induced crosslinking by incubation of cell lysates with $CuCl_2$ in the presence of ATP or the non-hydrolyzable ATP analog AMP-PNP. Provision of ATP, which is likely rapidly hydrolyzed to ADP and P_i by proteasomal ATPases (Smith et al., 2011), favors the s1 state in cryo-EM studies, whereas AMP-PNP yields only the s3 state (Unverdorben et al., 2014; Wehmer et al., 2017).

Anti-V5 immunoblotting of proteins separated by non-reducing SDS-PAGE revealed a loss of the Rpn7-V5 monomer and the appearance of a prominent higher molecular mass species in the ATP-containing lysates (Figure 1C). This species was seen only if both proteins contained the engineered cysteine residues, and was eliminated by the reducing agent DTT, consistent with a disulfide crosslink. Importantly, crosslinking of the same lysates prepared with AMP-PNP instead of ATP resulted in a near-complete loss of the crosslink. A similar effect was observed with the slowly hydrolysable ATP analog ATPγS, which also promotes the activated states of the proteasome (Śledź et al., 2013), and with a second pair of residues located in a different region of the proteasome (Figures S1B–S1D), supporting the notion that these crosslinks reported on the s1 state.

The archaeal homomeric homolog of the proteasomal ATPase ring, PAN, has two high- and two low-affinity sites for ATP (K_d ~0.5 μM and ~113 μM, respectively), and similar biphasic nucleotide binding was suggested for the yeast RP (Smith et al., 2011). To investigate the relationship between nucleotide concentration and conformational state of the eukaryotic proteasome, we tested the impact of increasing concentrations of ATPγS on s1 reporter crosslinking. We used ATPγS because it most closely resembles ATP but minimizes hydrolysis that may lead to conformational shifting. We did not obtain reliable crosslinking with concentrations of nucleotide ≤100 μM (not shown), which may reflect the dependence of 26S proteasomes on ATP for structural stability (Kleijnen et al., 2007). Overall, crosslinking was reduced substantially in the presence of ATPγS (Figure 1D) compared to ATP.

(B) Whole cell extracts (WCE) from WT cells or cells harboring the Rpn7-D123C (*rpn7-C*) or Rpt2-R407C (*rpt2-C*) substitutions were analyzed by native PAGE-immunoblotting or in-gel peptidase assay. The positions of RP_2CP, RP_1CP, RP, CP, and Blm10-CP are shown.

(C) Crosslinking of Rpn7 and Rpt2 requires engineered cysteines and is regulated by nucleotide. Crosslinking was induced in the presence of 2 mM of the indicated nucleotide. For the last lane, the WCE was incubated with DTT prior to loading.

(D) Nucleotide titration reveals additional state-switching at high concentrations of ATPγS. Crosslinking was conducted as above in the presence of the indicated ATP or ATPγS concentrations. The 4 mM ATP sample was loaded on both gels for normalization. Quantitation of crosslinking (n = 4) is shown to the right (two-way ANOVA with Sidak's multiple comparisons test). NS, not significantly different; *p < 0.001; **p < 0.0001.

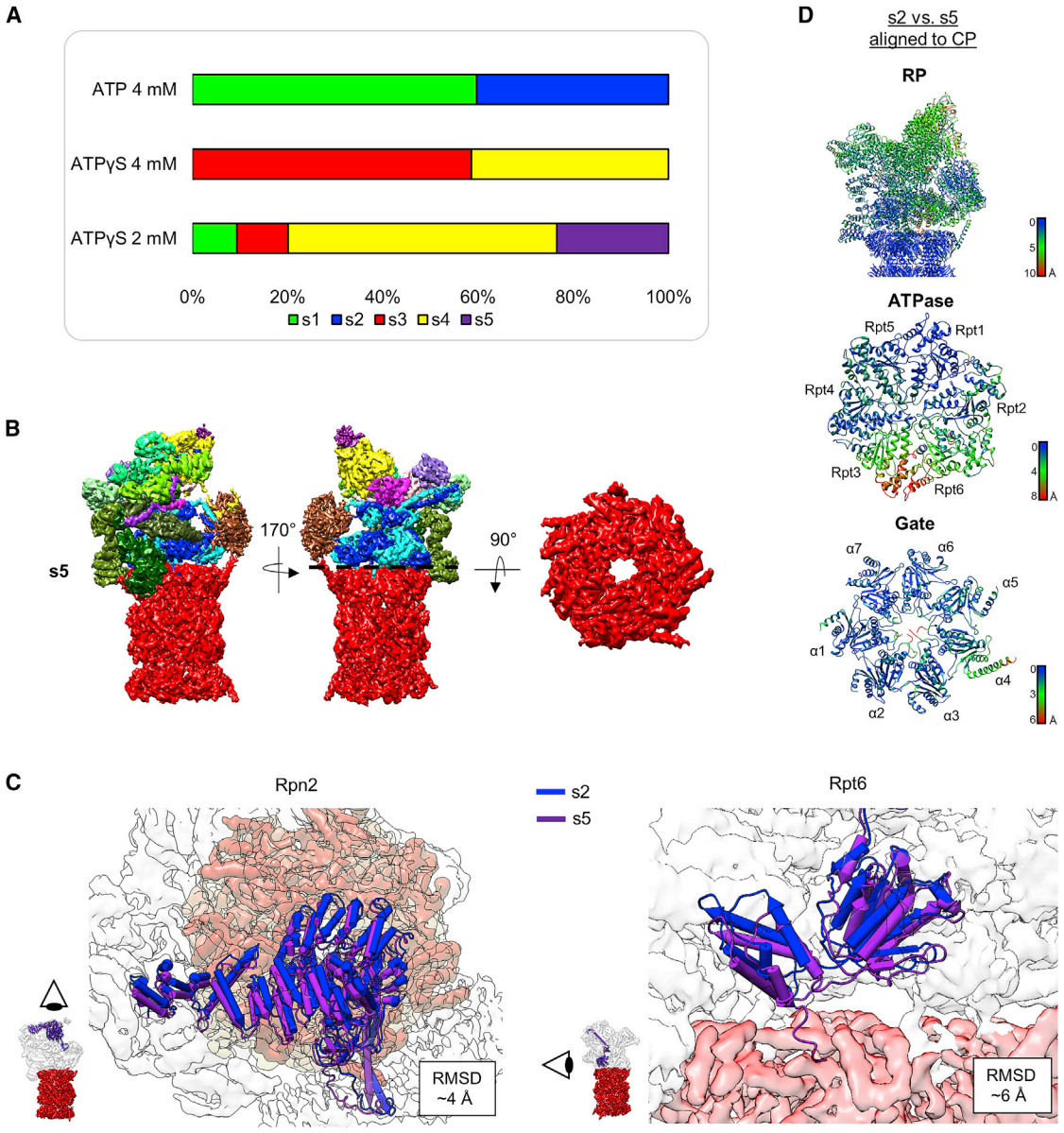

Figure 2. Titration of ATPγS Reveals the s5 Open-Gate Conformation

(A) The 26S proteasome state distribution depends on nucleotide conditions.

(B) Cryo-EM reconstruction of the 26S proteasome s5 state at 4.9 Å resolution with top view of the CP. Colors are as follows: CP (red), Rpt1, Rpt6, Rpt4 (blue), Rpt2, Rpt3, Rpt5 (cyan), Rpn1 (brown), Rpn2 (yellow), Rpn3, Rpn5, Rpn6, Rpn7, Rpn9, Rpn12 (shades of green), and Rpn8, Rpn10, Rpn11, Rpn13, Sem1 (shades of purple). No density is observed for the CP gate.

(C) Comparison of Rpn2 and Rpt6 in the s2 (EMD-3535; blue) and s5 (purple) states. The density of the s2 state is shown in gray and the CP in light red. The CP densities were aligned for comparison.

(D) Residue-wise root-mean-square deviation (RMSD) (in Å) of the 26S proteasome, the AAA+ ATPase and the gate between the s5 and s2 states.

Although some small fluctuations were evident, the crosslinking efficiency was rather stable at ATPγS concentrations between 0.5 and 2 mM, consistent with potential saturation of both low- and high-affinity nucleotide sites (Kim et al., 2015; Smith et al., 2011). However, a small but reproducible further loss of crosslinking was observed at concentrations ≥4 mM ATPγS (Figure 1D), suggesting additional conformational rearrangements may be taking place at high ATPγS.

Cryo-EM Structures in the Presence of ATPγS

To further address the influence of nucleotide concentration on proteasome conformation, we analyzed cryo-EM structures of the 26S proteasome in the presence of different concentrations of ATPγS. Analysis of proteasomes purified in 4 mM ATPγS revealed a higher abundance of the s3 and s4 activated states (Figure 2A). The s1 ground state was not observed, which is in agreement with the minimal s1 in the crosslinking results

(Figure 1D). At 2 mM ATPγS, the most abundant state was s4, whereas the two least abundant states were s1 and s3. The distribution shows similar trends as our previous study (Unverdorben et al., 2014), although some variance in abundances was noted. This may be due to differences in sample preparation, or more likely, to improved resolution and particle classification as compared to the previous study. In any event, the remaining ~23% of particles belonged to an as-yet unassigned proteasome state, which we designate s5 (Figures 2A and 2B). This distribution was not appreciably further altered by provision of a linear ubiquitinated model substrate, likely due to the strong influence of ATPγS on proteasome conformation (Figures S2D and S2E).

The particles from each state were further processed as described previously (Wehmer et al., 2017) to obtain refined EM maps of the s3, s4, and s5 states with global resolutions of 5.4, 4.5, and 4.9 Å, respectively (Figures 2B, S2C, S2F, and S2G). A root-mean-square deviation (RMSD) comparison of the s5 structure shows strong similarity to s2, save for a slight movement of specific subunits, such as Rpn2 by 4–6 Å (Figures 2C, 2D, and S2H). The ATPase ring of s5 adopts the overall conformation of s2, with the largest changes seen in Rpt3 and Rpt6. Rpt6 is shifted downward toward the CP by ~6 Å (Figures 2C and 2D). Whereas the overall structures of s2 and s5 states are highly similar, the s5 state clearly has an open gate, which allows for s5 and s2 to be discriminated (Figure 2B).

Non-equivalent Contributions of ATPases to Proteasome Conformational Dynamics

The resolution of these models did not allow us to determine the nucleotide states of the ATPases, so we used a genetic approach to assess the impact of individual ATP-binding events on proteasome conformational distribution. We first substituted glutamine for the conserved Walker B glutamate into each ATPase in yeast (*rpt-EQ*). This mutation prevents ATP hydrolysis by that subunit, thereby enriching the ATP-bound state. Although some enzymological characterization of recombinant proteasomal base EQ mutants has been performed (Beckwith et al., 2013), the impacts of these mutations on organismal health has not been evaluated. We systematically introduced EQ mutations into each ATPase in yeast by plasmid shuffle and tested the ability of the EQ allele to support viability upon eviction of the plasmid bearing the wild-type (WT) *RPT* allele on 5-fluoroorotic acid media (Figures 3A–3C). Four of the six mutants, *rpt2-EQ*, *rpt3-EQ*, *rpt5-EQ*, and *rpt6-EQ*, were viable, albeit with increasing growth defects in the order *WT* ≈ *rpt2-EQ* > *rpt3-EQ* > *rpt6-EQ* >> *rpt5-EQ*. The *rpt2-EQ* mutant was particularly well-tolerated, with no apparent growth defect even at elevated temperature (Figure S3A). The *rpt1-EQ* and *rpt4-EQ* mutations were lethal, and *rpt5-EQ* cells were too sick to culture reliably for additional experiments. No major structural or assembly defects were evident in proteasomes from *rpt2-*, *3-*, and *6-EQ* cells by native PAGE (Figure 3D), indicating the growth defects in the *rpt3-EQ* and *rpt6-EQ* mutants likely resulted from a proteolytic defect. Slightly elevated levels of double- and single-capped proteasomes (RP_2CP and RP_1CP) were evident in the *rpt6-EQ* mutant, likely due to homeostatic upregulation of proteasome synthesis to compensate for impaired activity (Ju and Xie, 2004; Xie and Varshavsky, 2001). In agreement, the steady-state levels of polyubiquitinated proteins in these mutants closely paralleled the severity of the growth defects (Figure 3E), with a substantial accumulation in *rpt6-EQ* cells.

We next introduced the *rpt2-EQ*, *rpt3-EQ*, and *rpt6-EQ* mutations into cells harboring the s1 crosslink reporter alleles and measured the abundance of the s1 conformation via crosslinking. Proteasomes harboring the *rpt2-EQ* mutation were as efficiently crosslinked as WT in the presence of ATP (Figure 4A), consistent with a minimal impact of the *rpt2-EQ* mutation on proteolysis *in vivo*. Crosslinking was also similar between *RPT2* and *rpt2-EQ* in the presence of AMP-PNP, indicating that nucleotide binding by Rpt2 had no net impact on the distribution between s1 and the activated (s2–s5) states. In contrast to the *rpt2-EQ* mutation, both *rpt3-EQ* and *rpt6-EQ* mutations caused a 3- to 4-fold decrease in crosslinking in the presence of ATP (Figures 4B and 4C), suggesting that the nucleotide binding by Rpt3 or Rpt6 enriches the activated states. This crosslinking was further decreased by provision of AMP-PNP. This likely reflects the impact of nucleotide binding at additional site(s) within the ring and further supports the notion that multiple nucleotide-binding events can contribute cooperatively to conformational reorganization (Figure 1D).

To acquire additional insight into the roles of individual ATPases, we performed cryo-EM analysis in the presence of ATP on *rpt-EQ* proteasomes. Each EQ mutant caused a distinct redistribution of conformational states (Figure 4D). The s2 state, which accounts for ~40% of particles in WT proteasomes, was absent in all datasets, suggesting it is generally disfavored by binding ATP, at least to the three ATPases assayed. Of the three EQ mutants, only *rpt6-EQ* increased the total percentage of proteasomes in activated states. In the *rpt2-EQ* proteasomes, consistent with the crosslinking results, the s1 state was near-equally populated as for WT proteasomes and the s2 state was replaced by the activated s5 (~12%) and s4 (~30%) states (Figure 4D). For *rpt6-EQ* proteasomes, the abundance of the s1 state was reduced to ~42% and was complemented by the appearance of the s5 (~17%) and s4 (~41%) open-gate states (Figure 4D). In *rpt3-EQ* proteasomes, we observed a previously unidentified conformational state that made up the entire non-s1 population (~46%), which we termed s6 (Figure 4E). Overall, the s6 state resembled the s3 state (Figure S4), with the major distinguishing feature of an open gate and a different ATPase subunit geometry (discussed below). The reason for the discrepancy between the crosslinking (Figure 4B) and EM analysis for *rpt3-EQ* proteasomes may reflect altered positions of the reporter cysteines not obvious by EM, but sufficient to prevent efficient crosslinking. In any event, these results together suggest that ATP binding by proteasomal ATPases disfavors the s2 state, and promotes the open-gate s4, s5, or s6 states. In agreement, the peptidase rates of the three *rpt-EQ* proteasomes were elevated 2- to 3-fold compared to WT proteasomes (Figure 4F).

Comparison of Proteasomal Nucleotide-Binding Pockets

Despite the anisotropic local resolution, EM densities of the bulky side chains were well resolved in the subunits of the CP and several RP subunits, including the AAA+ ATPase subunits. We thus applied a combined Rosetta and molecular dynamics

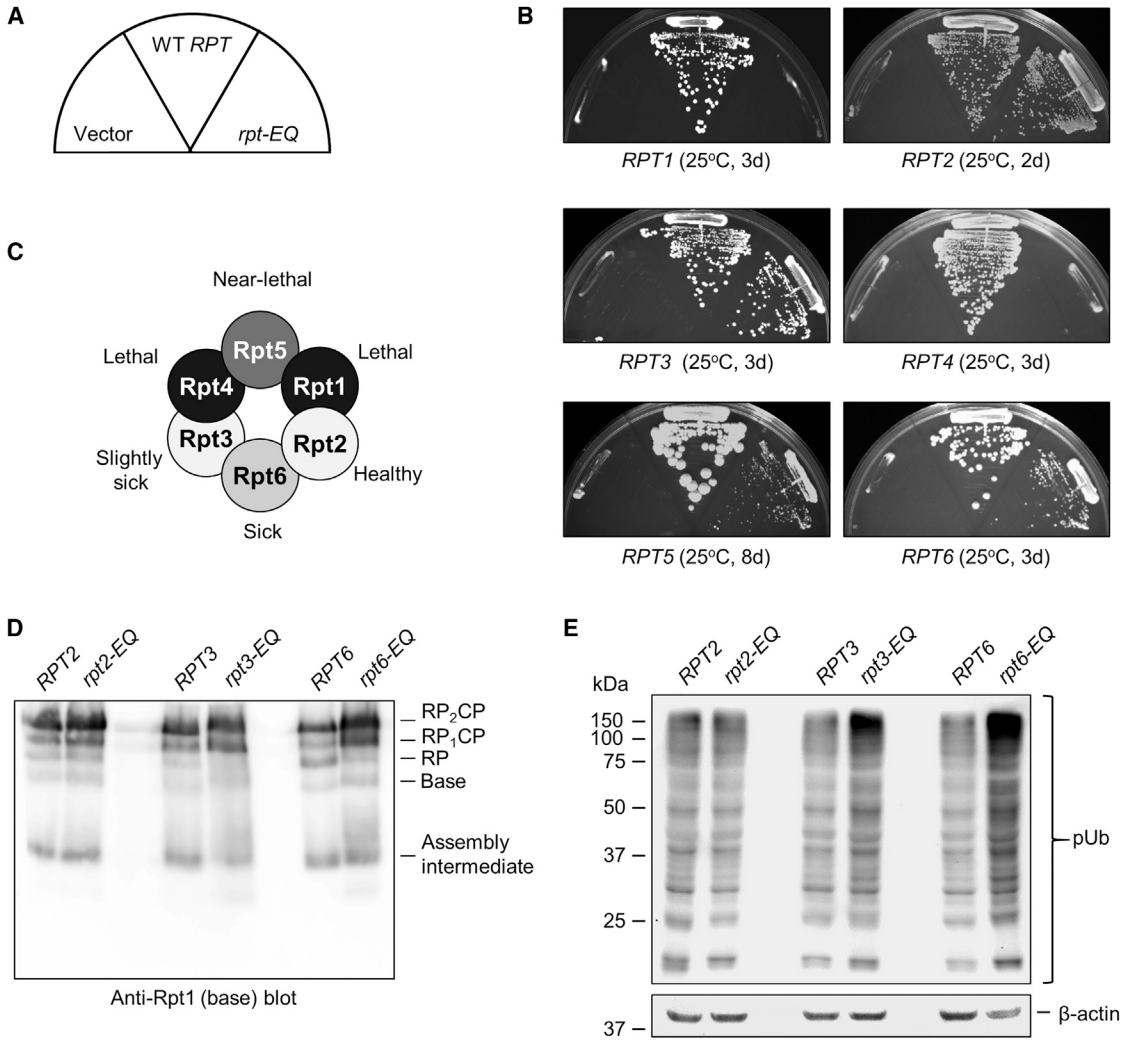

Figure 3. Walker B Mutations Differentially Impact Proteasome Function and Viability in Yeast

(A) Arrangement of plasmid-bearing *rpt* deletion strains shown in (B).

(B) Walker B mutation (EQ) of the proteasomal ATPases is differentially tolerated in yeast. Cells lacking the indicated *RPT* gene and carrying a WT *RPT*/*URA3* plasmid were transformed with empty, *RPT*, or *rpt-EQ* plasmids. Cells were struck on 5-fluoroorotic acid medium as in (A) to select for cells that had lost the original *RPT*/*URA3* plasmid, and incubated at 25°C for the indicated times.

(C) Summary of growth phenotypes of yeast *rpt-EQ* mutants.

(D) Efficient proteasome formation in *rpt-EQ* cells. Native gel immunoblot analysis of the indicated strains is shown.

(E) Accumulation of polyubiquitin in *rpt3*- and *rpt6-EQ* cells.

flexible fitting approach, which was previously shown to improve such models (Lindert and McCammon, 2015; Song et al., 2013). These improved models made the following structural analyses possible, starting with the nucleotide-binding pockets. As previously reported, we identified six fully occupied nucleotide pockets in all conformational states (Figure S5A) (Chen et al., 2016; Huang et al., 2016; Schweitzer et al., 2016; Wehmer et al., 2017). Although the bound nucleotide cannot be confidently assigned, analysis of two key features of the binding pocket allows discernment of three distinct pocket configurations (Figure 5). First, we measured the pocket distance from the end of the H10 helix connected to the pore-2 loop to the N-terminal tip of the Walker A motif located at the beginning of the H6 helix to distinguish engaged or open pockets (Figures 5C, 5D, and S5B) (Wehmer et al., 2017). In the engaged pocket, this distance is ~15 Å or smaller, whereas in the open pocket the distance is 18 Å or greater. This pocket distance often correlates with the second feature: the position of a well-conserved phenylalanine at the end of the H10 helix in each Rpt subunit (Figures 5A and 5B). In an engaged Phe-cluster, the conserved phenylalanine interacts with an arginine and phenylalanine in β2 and β3 strands of the counter-clockwise neighboring subunit. In contrast, in an open Phe-cluster, the phenylalanine is flipped away from the neighboring subunit and instead points toward the H9 helix of the same ATPase subunit, yielding a larger gap between Rpt subunits.

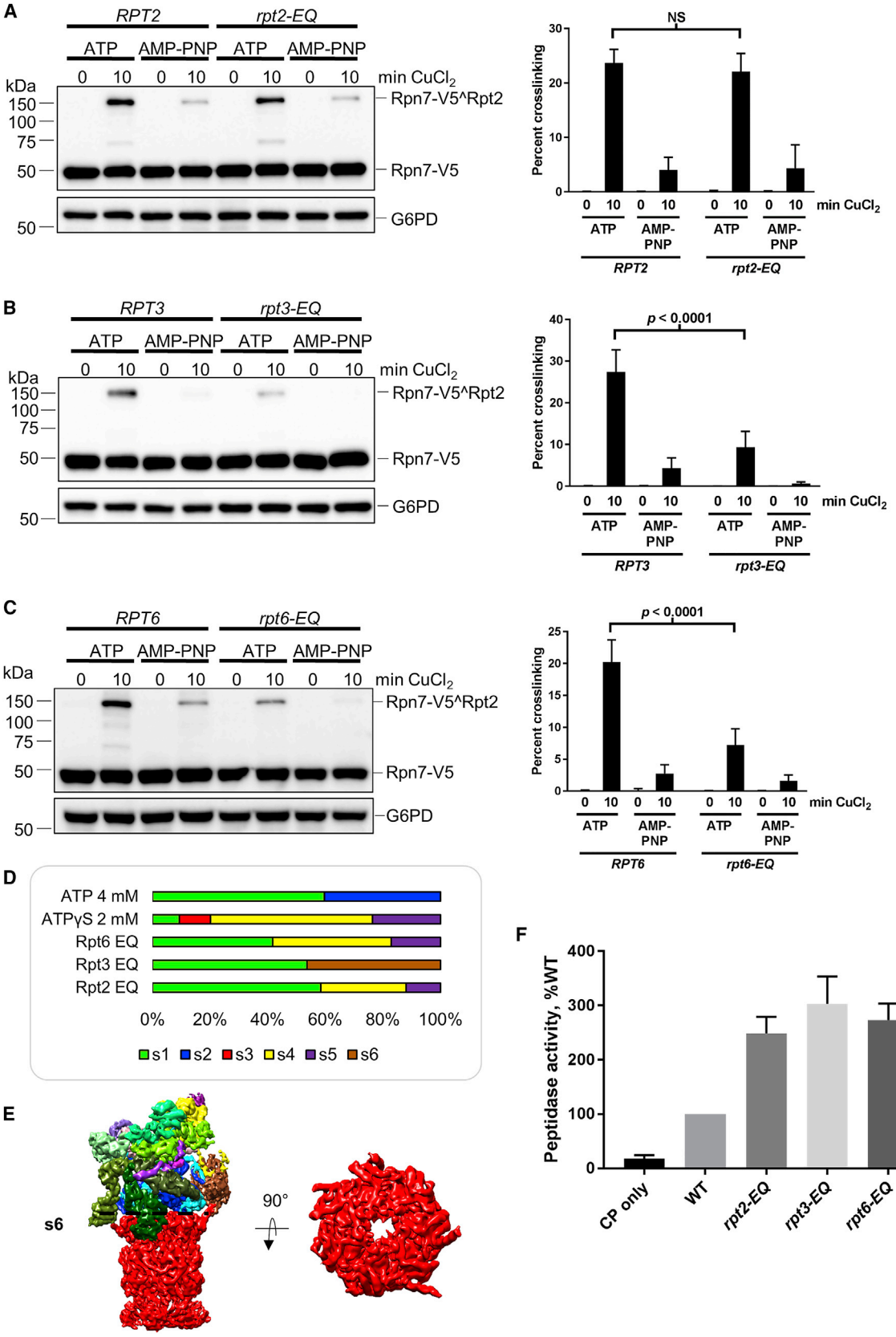

(legend on next page)

By applying these measurements to the Rpt subunits of each conformational state, a total of three different types of nucleotide pocket can be identified. A pocket is either open both in terms of the pocket distance and the Phe-cluster (open), it can have an engaged pocket but an open Phe-cluster (intermediate), or finally it can be completely engaged in both factors (engaged). The differentiation of open and engaged pockets was additionally supported by hierarchal clustering of masked nucleotide pocket maps (Figure S5C). Each state is hereby characterized by a specific arrangement of pocket states (Figure 5E). In s1, s2, and s5, the same arrangement is observed, with engaged pockets in Rpt1, Rpt5, Rpt4, and Rpt3 followed by an open Rpt6 pocket and an intermediate Rpt2 pocket in clockwise position. In contrast, s3 displays three engaged pockets (Rpt4, Rpt3, and Rpt6) followed by two open pockets (Rpt1 and Rpt5), and by one intermediate pocket (Rpt2). Intriguingly, this pattern is permuted one subunit counterclockwise from s3 to s6 and again from s6 to s4.

Docking of the Rpt1 and Rpt6 C Termini Promotes Gating of the CP

The conserved HbYX motifs of Rpt2, Rpt3, and Rpt5 were originally proposed to mediate RP-dependent CP gating based on analogy to the archaeal proteasome and biochemical studies using high concentrations of synthetic HbYX peptides (Rabl et al., 2008; Smith et al., 2007). Yet, recent cryo-EM studies of the proteasome have shown docking of the termini of all three HbYX subunits in both closed- and open-gate states (Chen et al., 2016; Wehmer et al., 2017). To clarify this apparent discrepancy, we first analyzed the density at the interface between the CP and the RP in our refined EM reconstructions of s1–s6. As observed previously, the C termini of the three HbYX-containing subunits were stably docked into the α ring in the closed-gate states (s1, s2, and s3). These subunits were also stably docked in the open-gate states (s4–s6), but two additional densities corresponding to the C termini of Rpt1 and Rpt6 docked into the α pockets were also observed (Figures 6A and S6A). Although the Rpt1 and Rpt6 C termini do not contain a HbYX motif, the sequences are highly conserved (Figures S6B and S6C). In the s4 state solved with BeF_x, we observed the Rpt6 C terminus but not the Rpt1 C terminus, probably due to limited resolution (Wehmer et al., 2017). Although we observed a minimal extra density for the Rpt6 C terminus in the s3 state, the gate was still occluded (Figure 6A), implying that the Rpt6 tail either is not firmly docked or is not sufficient to open the gate.

To test our hypothesis that the Rpt1 and Rpt6 tails promote CP gating, we utilized yeast mutants lacking the C-terminal amino acids of Rpt1 or Rpt6. These truncations prevent efficient docking of the Rpt tail into the CP pockets (Park et al., 2009, 2011). We then evaluated the effects of these truncations on RP-dependent gating of the CP via an in-gel peptidase assay using the fluorogenic substrate suc-LLVY-AMC. This allowed us to distinguish peptidase activity specifically arising from RP-capped CPs (Figure 6B). To account for a mild assembly defect resulting from the *rpt6-Δ1* mutation (Park et al., 2009, 2011), we normalized peptidase activity to proteasome abundance in immunoblots of the same extracts (RP_2CP; Figure 6B). Full proteasomes from WT cells as well as *rpt1-Δ1* cells showed robust peptidase activity, evidenced by accumulation of bright fluorescence. In contrast, *rpt6-Δ1* proteasomes were slightly less active. Importantly, and consistent with our EM results, peptidase activity was decreased nearly 80% in proteasomes from *rpt1-Δ1 rpt6-Δ1* yeast (Figure 6B), strongly supporting a cooperative role for the Rpt1 and Rpt6 tails. This finding was mirrored by a strong synthetic growth defect in *rpt1-Δ1 rpt6-Δ1* yeast (Figure 6C). Together, these data support a model in which the C termini of Rpt1 and Rpt6 cooperatively drive gate-opening via interactions with the surface of the CP.

Structural Basis of Gating by C-Terminal Insertions of Rpt1 and Rpt6

To understand how Rpt1 and Rpt6 promote gating, we segmented density originating from the N-terminal extensions of the α subunits and modeled this region. In the closed gate conformations (s1–s3), the N-terminal segments of three α subunits, α2, α3, and α4, lay down horizontally to form the central gate, whereas the remaining α subunit N termini point upward toward the ATPase ring. A tight cluster is formed by Asp7 of α3 with Arg6 and Tyr4 of α4 in the center of the gate, as previously observed (Groll et al., 2000). However, we observe an additional interaction of Phe7 from α2 with these residues. Phe7 appears to nucleate this cluster to keep the α3 N terminus in place and secure the gate over the CP pore (Figure 7A). Although many of the N-terminal residues of the seven α subunits are highly conserved both among each other and with the archaeal subunits, a Phe at position 7 is found only in the eukaryotic α2, suggesting a unique function in reinforcing the central gate. In agreement, the archaeal CP displays a more disordered gate (Förster et al., 2005; Groll et al., 2000). In further support, introduction of the nonconservative α2(F7A) mutation caused resistance to the heavy metal Cd^{2+}, a phenotype characteristic of open-gate mutants of the CP (Figure 7C) (Kusmierczyk et al., 2008). This was not observed for cells harboring the conservative α2(F7Y) mutation alone, but combination with the nonconservative α3(Y24A) mutation in the adjacent α3 H0 helix led to weak Cd^{2+} resistance, consistent with the α2 N terminus serving as a linchpin for the closed gate via interaction with the N terminus of α3.

During the transition from the closed to the open gate configuration, the N termini of α2, α3, and α4 undergo a large

Figure 4. Walker B Mutations Differentially Impact Proteasome Conformational Distribution

(A–C) Crosslinking in WCEs from *rpt2-EQ* (A), *rpt3-EQ* (B), or *rpt6-EQ* (C) cells or WT controls in the presence of ATP or AMP-PNP. Quantitation of crosslinking ($n \geq 3$ independent replicates) is shown to the right and was analyzed by two-way ANOVA with Sidak's multiple comparisons test. NS, not significantly different.

(D) The proteasome state distribution of the three *rpt-EQ* mutants. The 4 mM ATP and 2 mM ATPγS state distributions for WT proteasomes (Figure 2A) are shown for reference.

(E) Cryo-EM reconstructions at a resolution of 6.1 Å of the s6 state. The 26S proteasome is colored as in Figure 2B.

(F) *rpt-EQ* proteasomes show elevated peptidase activity. Peptidase activity toward suc-LLVY-AMC is expressed as % of WT proteasomes. Error bars indicate SD (n = 3).

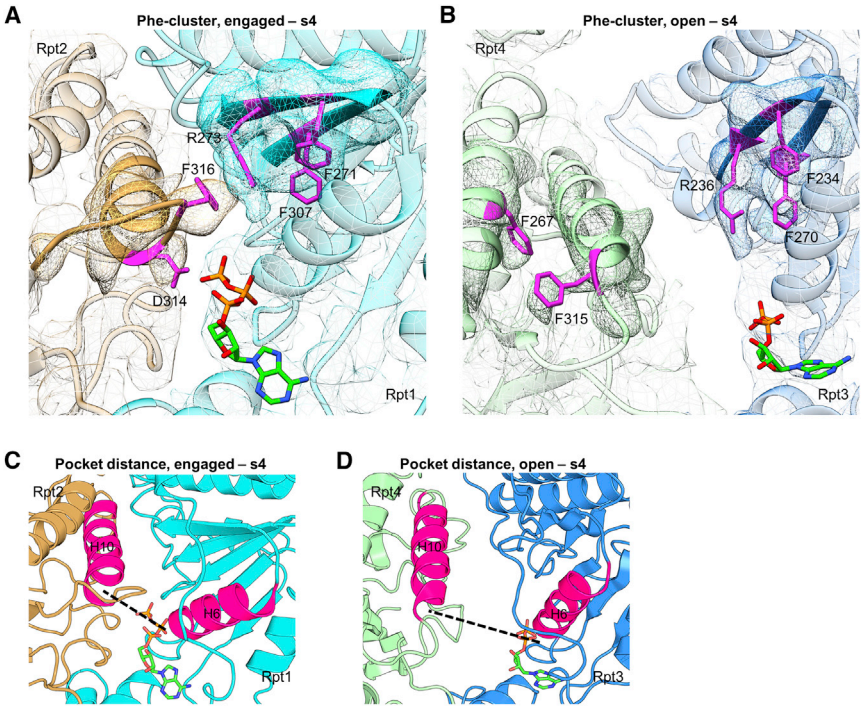

Figure 5. Phe-Clustering between Rpt Subunits Reveals Stepwise Movement during Activation

(A) In an engaged Phe-cluster in s4, the Phe316 of Rpt2 at the H10 helix bridges toward Phe271, Phe307, and Arg273 of the neighboring subunit Rpt1.

(B) In an open Phe-cluster, Phe315 of Rpt4 at the H10 helix points toward the interior of Rpt4. The EM density of of the ATPase subunits is shown as a mesh, and the Phe cluster is highlighted by a darker colored mesh.

(C and D) Comparison of the pocket distance in an engaged (C) and an open pockets (D). The pocket distance is $\leq$15 Å in an engaged pocket (C), whereas the distance is $\geq$18 Å in an open pocket (D).

(E) Overview of the conformational states of the nucleotide binding pockets in all six states. White shading indicates an "open" conformation with an open Phe-cluster and an open pocket, light blue indicates an "intermediate" conformation with an open Phe-cluster and an engaged pocket, and dark blue indicates an "engaged" conformation with an engaged Phe-cluster and an engaged pocket.

conformational change from a horizontal to a vertical arrangement. Thereby, the N termini form a cluster with two conserved tyrosines, a proline and one aspartate (YD-P-Y motif) at the interface between two α subunits at the periphery of the CP pore (Figures 7B, main panel, and S7C). These conserved clusters can also be found between α5, α6, and α7 in both the closed and open gate (Figure S7D). In contrast, α1-α2 forms an atypical tyrosine-proline-tyrosine cluster in the open gate state (Figure 7B, lower panel), and Phe7 of α2 prevents Tyr21 of α1 from hydrogen bonding with Ser6 of α2.

In all open gate states, both a proline in α2 and the H0 helix of α3 are repositioned compared to the closed gate states (Figure S7E). Importantly, the tails of Rpt1 and Rpt6, when inserted into the respective α4-α5 and α2-α3 pockets, are perfectly positioned to promote these movements, disrupting the tight clustering in the central gate and triggering opening of the gate. In the s3 state, where we also observe a minimal density for the Rpt6 C terminus, these movements cannot be identified, consistent both with an occluded gate and with the hypothesis that the Rpt6 terminus is not firmly docked in the s3 state. Taken together, these data support a mechanism by which insertion of the Rpt6 and Rpt1 C termini into the α ring promotes reorganization of the gate via displacement of the α2-Phe7-centered linchpin to release the termini of α2, α3, and α4 and promote access to the peptidase chamber.

DISCUSSION

Here, we reveal the impact of individual ATP-binding events on proteasome conformational dynamics and report two additional open-gate states. These structures revealed key roles for the Rpt1 and Rpt6 C termini in opening the CP gate in the context of the proteasome holoenzyme. The observation that the Rpt1 and Rpt6 termini flank the α subunit N termini responsible for forming the gate, and upon insertion, reposition key structural elements of these N termini that nucleate them over the CP pore provides a clear allosteric mechanism of CP gating by the RP. In conjunction with previous studies demonstrating that gating depends on intact HbYX motifs of Rpt2, Rpt3, and Rpt5 (Smith et al., 2007), we propose that efficient CP gating is triggered by docking of the three HbYX subunits, followed by docking of Rpt1 and Rpt6 (Figure 7D). This model unites the dependence of gating on HbYX motifs with the seemingly paradoxical observation that all three HbYX motifs are stably docked in closed gate structures of the proteasome. Further, the finding that the *rpt6-EQ* mutation alone is sufficient to convert ~60% of proteasomes to an open-gate state (Figure 4D) is consistent with a key role for this subunit in activating the proteasome and in transmitting the nucleotide state of the ATPase ring to the CP.

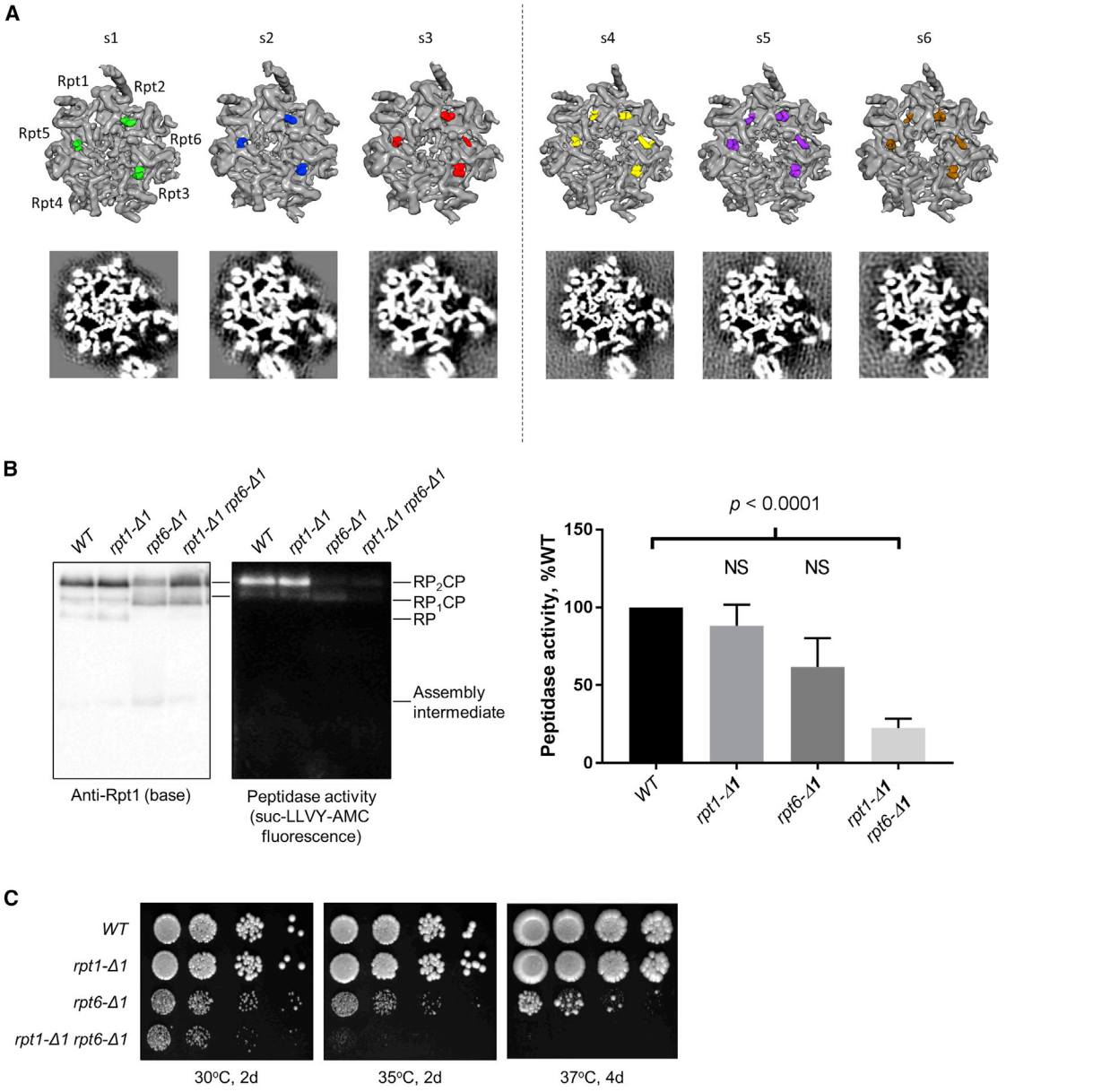

Figure 6. RP-Dependent Gating of the CP

(A) Insertion of Rpt C-terminal tails into CP α ring pockets. Top view of the CP from each of the six states, where the CP is depicted in gray with colored C-terminal Rpt densities inserted into the CP. All densities were filtered to 6.1 Å. Densities to the left of the dashed lines are EM maps with a closed gate (visible density in the center of the CP) and to the right are densities with an open gate (no density in the center of the CP). The C-terminal Rpt density is depicted in green for s1 (EMD-3534), blue in s2 (EMD-3535), red in s3, yellow in s4, purple in s5, and brown in s6. Under the top panel, slices of the EM density at a similar position for each state are shown.

(B) The Rpt1 and Rpt6 C termini cooperate to promote gate opening. WCEs of the indicated yeast strains were separated by nondenaturing PAGE before measurement of peptidase activity as above or by anti-Rpt1 immunoblotting. There was slight rescue of the *rpt6-Δ1* assembly defect in the *rpt1-Δ1 rpt6-Δ1* mutant in two independently isolated clones. For quantitation of peptidase activity (right), AMC fluorescence was normalized to the Rpt1 signal for double-capped proteasomes (n = 4; one-way ANOVA with Dunn's multiple comparisons test). NS, not significantly different.

(C) Enhanced heat sensitivity in the *rpt1-Δ1 rpt6-Δ1* double mutant.

Our conformation-specific crosslinking and cryo-EM data indicate that the conformational landscape of the proteasome is influenced both by the nucleotide concentration as well as by nucleotide binding to individual ATPases. Previous *in vitro* analyses of individual ATPase mutants showed that the six subunits contribute differently to substrate unfolding and translocation (Beckwith et al., 2013; Kim et al., 2013; Lee et al., 2012; Rubin et al., 1998). Our results demonstrate these subunits are

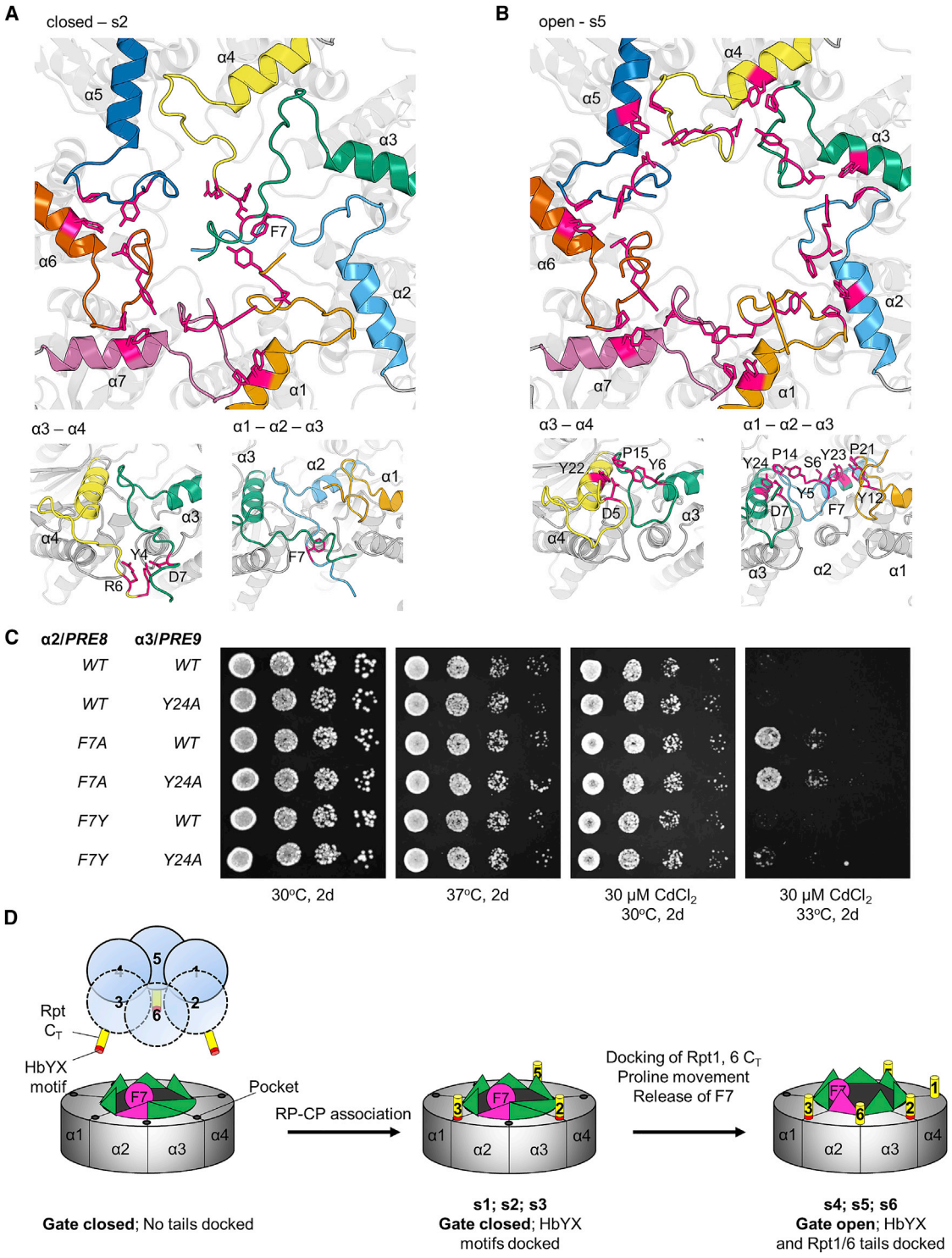

Figure 7. A Conserved Cluster of Aromatic Residues Controls Gate-Opening by the RP

(A and B) Detailed view of the closed gate of s2 (A) and the open gate of s5 (B). Each α subunit is colored as follows: α1, light orange; α2, light blue; α3, dark green; α4, yellow; α5, dark blue; α6, dark orange; and α7, light pink. The key side chains are colored in magenta. Close-up views of the important cluster residues of the N termini of α1–α4 are shown in the lower panels. In the open gate (B), a canonical cluster is formed between α3 and α4 (left) and α2 and α3 (right), whereas an atypical cluster is formed between α1 and α2 (right).

(C) Mutation of α2-F7 promotes Cd^{2+} resistance, a hallmark of proteasomal gate mutants.

(D) Schematic model of CP gating. See text for details.

further distinguished by their impacts on the conformational distribution of the proteasome. The nucleotide binding pockets of related homohexameric AAA+ ATPases have recently been characterized at near-atomic resolution (Banerjee et al., 2016; Puchades et al., 2017). One such study showed that the Phe cluster near the nucleotide binding pocket allosterically regulates pore-loop movement upon ATP hydrolysis (Puchades et al., 2017). Our analysis revealed three configurations of the nucleotide-binding pocket that are distinguished by a combination of the pocket distance and the Phe cluster. We note that the engaged, intermediate, and open pocket configurations in the heterohexameric proteasomal ATPase ring resemble the ATP-bound, ADP-bound, and empty configurations, respectively, of these simpler homomeric ATPases. Substrate translocation is believed to follow a sequential nucleotide-driven translocation, by which the ATPase pocket architecture is shifted counterclockwise by one subunit upon ATP hydrolysis by the trailing engaged subunit (Gates et al., 2017; Monroe et al., 2017; Puchades et al., 2017). An identical subunit shift can be envisioned from s3 to s6 to s4 for the proteasome (Figure S7F), implying a conserved mechanism for sequential nucleotide-driven translocation.

The lethality of the *rpt1-EQ* and *rpt4-EQ* mutants, and near-lethal phenotype of the *rpt5-EQ* mutant, suggests that ATP hydrolysis by these ATPases is especially important for proteasome function *in vivo*. This observation is in some contrast to a previous *in vitro* study (Beckwith et al., 2013) that reported near-complete loss of substrate degradation in rpt3-, rpt4-, and rpt6-EQ mutants, and only partial defects in rpt1- and rpt5-EQ mutants. Although the reason for this discrepancy is unknown, we note that the *in vitro* analysis evaluated the impact of these mutations on a single substrate, whereas the cell-based data presented here reflects the net impact on degradation of all cellular substrates. Thus, one intriguing question arising is whether the individual ATPases differentially contribute to turnover of particular substrates.

The minimal disruption to protein degradation *in vivo* and to proteasome conformational distribution *in vitro* by the *rpt2-EQ* mutation is consistent with *in vitro* studies reporting minimal impact on substrate degradation (Beckwith et al., 2013) and with a major function of Rpt2 in nucleotide-dependent priming of the CP for gating (Köhler et al., 2001; Rubin et al., 1998). Rpt2's position within the ATPase ring between Rpt1 and Rpt6 is optimal to communicate with these critical ATPases involved in CP gating and suggests that loading of Rpt2 with ATP may be required to promote tail insertion into the CP by Rpt1 and/or Rpt6. In this way, nucleotide binding by Rpt2 may be one of the initiating events in substrate unfolding, and serve to couple initiation of unfolding to CP gating to ensure efficient translocation. This gating function would likely be most important during the initial penetration of the CP by substrate, as the substrate could help to hold the gate open for further translocation as ATP hydrolysis proceeds around the ring.

Although previous studies revealed that HbYX motif insertion is necessary for gate-opening (Beckwith et al., 2013; Kim and DeMartino, 2011; Smith et al., 2007), recent structural studies of 26S proteasomes have demonstrated stable insertion of the three HbYX motifs into the α ring even in closed-gate states, indicating that these insertions are not sufficient to promote or maintain an open gate. Although CP gating can be stimulated with individual HbYX-containing peptides *in vitro* (Smith et al., 2007), EM analyses of isolated CP with such peptides has demonstrated nonselective binding to α pockets (Park et al., 2013), confounding interpretation of these peptide-based experiments. Our model of Rpt6- and Rpt1-dependent gating is supported by the following observations, made in the context of full proteasomes: (1) in the three open gate states, the Rpt6 and Rpt1 C termini are clearly detected at the α subunit interface in addition to the three constitutive HbYX motif insertions; (2) mutation of the Rpt6 and Rpt1 C termini synergistically compromises peptidase activity *in vitro* and causes a growth defect *in vivo*; (3) Rpt6 and Rpt1 C termini dock into pockets formed by the α2, α3, and α4 subunits critical for gate formation; and (4) insertion of the Rpt6 and Rpt1 C termini into their respective pockets repositions the H0 helices of α2–α4 from their positions in the closed-gate states in our open-gate structures. In agreement, the only currently reported open-gate state of the human proteasome displays some density for Rpt1 and Rpt6 termini at their cognate α ring pockets (Chen et al., 2016).

We observe that the amino acid clusters formed upon gate-opening by the RP are similar to those observed with other CP activators (Förster et al., 2005; Sadre-Bazzaz et al., 2010; Whitby et al., 2000; Yu et al., 2010). Interactions through the highly conserved α subunit YD(R)-P-Y motif is important for both open and closed gate conformations. Interestingly, the evolution of Ser6 for Asp and of Phe7 for Arg in the YD(R)-P-Y motif of α2 allows it both to stabilize the closed gate via interaction with the N-terminal extension of α3 and also to form an atypical open-gate cluster with the Pro-loop, which is shifted by ~3.5 Å upon insertion of the Rpt6 C terminus (Figure S7E).

It has been postulated that ATP binding by a given ATPase subunit drives insertion of its C-terminal tail into the CP to open the gate (Smith et al., 2007, 2011). Although we cannot discern the ATPase nucleotide states in our structures, our pocket analysis indicates that there is no absolute correlation between pocket configuration and the status of the gate. However, when either the Rpt1 or Rpt6 nucleotide-binding pocket is open, the gate is closed with a sole exception, the s5 state. Because the s2 and s5 states are highly similar to one another and because the ATPase ring in the s5 state shares the same binding pocket configuration as the closed-gate s2 state (Figure S7F), a comparison between these two is instructive. Interestingly, despite the open Rpt6 pocket in both the s2 and s5 states, Rpt6 is shifted downward significantly in the s5 state, which likely promotes tail insertion. Thus, in addition to the Rpt6 positioning in response to nucleotide binding, interactions with other subunits may regulate its gating function. Further studies will be necessary to determine how the insertion of ATPase tails is related to the nucleotide binding state of the ATPase ring and to the ATP-binding pocket configuration. However, the expanded knowledge of the conformational landscape and of gating by the ATPase ring will serve as a valuable framework for dissecting how these key functional events are mechanistically connected.

STAR★METHODS

Detailed methods are provided in the online version of this paper and include the following:

- KEY RESOURCES TABLE
- CONTACT FOR REAGENT AND RESOURCE SHARING
- EXPERIMENTAL MODEL AND SUBJECT DETAILS
  - Yeast strains and media
  - Plasmids
- METHOD DETAILS
  - Disulfide Crosslinking of Conformation-specific Proteasome Reporters
  - Native polyacrylamide gel electrophoresis
  - Measurement of peptidase activity
  - Production of anti-Rpn12 antisera
  - Immunoblot Analyses
  - Purification of Proteasomes
  - Data acquisition
  - Image processing
  - Single particle analysis
  - Model Building
  - Volume analysis of the nucleotide binding pocket
- QUANTIFICATION AND STATISTICAL ANALYSIS
- DATA AND SOFTWARE AVAILABILITY

SUPPLEMENTAL INFORMATION

Supplemental Information includes seven figures and two tables and can be found with this article online at https://doi.org/10.1016/j.celrep.2018.07.004.

ACKNOWLEDGMENTS

The authors thank William P. Tansey for anti-Rpt1 hybridomas. We also thank R. Fernandez Busnadiego, N.R. Wilson Eisele, and M. Wehmer for critical reading. This work was supported by start-up funds from the Florida State University College of Medicine and NIH (5R01GM118600 to R.J.T.) and by the German Science Foundation (Excellence Cluster CIPSM to W.B. and SFB-1035/Project A01 to W.B. and E.S.). E.S. is supported by Marie Curie Career Integration grant (PCIG14-GA-2013-631577).

AUTHOR CONTRIBUTIONS

R.J.T. and R.G.R. generated yeast strains and plasmids, performed all crosslinking experiments, and performed genetic analyses. R.J.T. characterized ATPase mutants and performed peptidase assays. M.R.E., A.S., I.N., and R.J.T. purified proteasomes. M.R.E., G.P., and J.M.P. performed the electron microscopy experiments. T.R. and M.R.E. constructed the structural models. M.R.E., T.R., F.B., and A.S. analyzed the EM data. M.R.E., W.B., R.J.T., and E.S. designed the research. M.R.E., E.S., and R.J.T. drafted the manuscript, and all authors provided feedback. R.J.T. and E.S. supervised the experiments.

DECLARATION OF INTERESTS

The authors declare no competing interests.

Received: March 30, 2018
Revised: June 8, 2018
Accepted: July 2, 2018
Published: July 31, 2018

SUPPORTING CITATIONS

The following references appear in the Supplemental Information: Lu et al. (2015); Martin et al. (2008).

REFERENCES

Aufderheide, A., Beck, F., Stengel, F., Hartwig, M., Schweitzer, A., Pfeifer, G., Goldberg, A.L., Sakata, E., Baumeister, W., and Förster, F. (2015). Structural characterization of the interaction of Ubp6 with the 26S proteasome. Proc. Natl. Acad. Sci. USA *112*, 8626–8631.

Banerjee, S., Bartesaghi, A., Merk, A., Rao, P., Bulfer, S.L., Yan, Y., Green, N., Mroczkowski, B., Neitz, R.J., Wipf, P., et al. (2016). 2.3 Å resolution cryo-EM structure of human p97 and mechanism of allosteric inhibition. Science *351*, 871–875.

Bard, J.A.M., Goodall, E.A., Greene, E.R., Jonsson, E., Dong, K.C., and Martin, A. (2018). Structure and function of the 26S proteasome. Annu. Rev. Biochem. *87*, 697–724.

Baumeister, W., Walz, J., Zühl, F., and Seemüller, E. (1998). The proteasome: paradigm of a self-compartmentalizing protease. Cell *92*, 367–380.

Beck, F., Unverdorben, P., Bohn, S., Schweitzer, A., Pfeifer, G., Sakata, E., Nickell, S., Plitzko, J.M., Villa, E., Baumeister, W., and Förster, F. (2012). Near-atomic resolution structural model of the yeast 26S proteasome. Proc. Natl. Acad. Sci. USA *109*, 14870–14875.

Beckwith, R., Estrin, E., Worden, E.J., and Martin, A. (2013). Reconstitution of the 26S proteasome reveals functional asymmetries in its AAA+ unfoldase. Nat. Struct. Mol. Biol. *20*, 1164–1172.

Bradford, M.M. (1976). A rapid and sensitive method for the quantitation of microgram quantities of protein utilizing the principle of protein-dye binding. Anal. Biochem. *72*, 248–254.

Chen, P., Johnson, P., Sommer, T., Jentsch, S., and Hochstrasser, M. (1993). Multiple ubiquitin-conjugating enzymes participate in the in vivo degradation of the yeast MAT alpha 2 repressor. Cell *74*, 357–369.

Chen, S., Wu, J., Lu, Y., Ma, Y.B., Lee, B.H., Yu, Z., Ouyang, Q., Finley, D.J., Kirschner, M.W., and Mao, Y. (2016). Structural basis for dynamic regulation of the human 26S proteasome. Proc. Natl. Acad. Sci. USA *113*, 12991–12996.

Finley, D., Chen, X., and Walters, K.J. (2016). Gates, channels, and switches: elements of the proteasome machine. Trends Biochem. Sci. *41*, 77–93.

Förster, A., Masters, E.I., Whitby, F.G., Robinson, H., and Hill, C.P. (2005). The 1.9 A structure of a proteasome-11S activator complex and implications for proteasome-PAN/PA700 interactions. Mol. Cell *18*, 589–599.

Gates, S.N., Yokom, A.L., Lin, J., Jackrel, M.E., Rizo, A.N., Kendsersky, N.M., Buell, C.E., Sweeny, E.A., Mack, K.L., Chuang, E., et al. (2017). Ratchet-like polypeptide translocation mechanism of the AAA+ disaggregase Hsp104. Science *357*, 273–279.

Geng, F., and Tansey, W.P. (2012). Similar temporal and spatial recruitment of native 19S and 20S proteasome subunits to transcriptionally active chromatin. Proc. Natl. Acad. Sci. U.S.A *109*, 6060–6065.

Goh, B.C., Hadden, J.A., Bernardi, R.C., Singharoy, A., McGreevy, R., Rudack, T., Cassidy, C.K., and Schulten, K. (2016). Computational methodologies for real-space structural refinement of large macromolecular complexes. Annu. Rev. Biophys. *45*, 253–278.

Groll, M., Bajorek, M., Köhler, A., Moroder, L., Rubin, D.M., Huber, R., Glickman, M.H., and Finley, D. (2000). A gated channel into the proteasome core particle. Nat. Struct. Biol. *7*, 1062–1067.

Guo, Q., Lehmer, C., Martinez-Sanchez, A., Rudack, T., Beck, F., Hartmann, H., Perez-Berlanga, M., Frottin, F., Hipp, M.S., Hartl, F.U., et al. (2018). In situ structure of neuronal C9orf72 Poly-GA aggregates reveals proteasome recruitment. Cell *172*, 696–705.

Guthrie, C., and Fink, G. (1991). Guide to yeast genetics and molecular biology. Methods Enzymol. *194*, 1–863.

Huang, X., Luan, B., Wu, J., and Shi, Y. (2016). An atomic structure of the human 26S proteasome. Nat. Struct. Mol. Biol. *23*, 778–785.

Humphrey, W., Dalke, A., and Schulten, K. (1996). VMD: visual molecular dynamics. J. Mol. Graph. *14*, 33–38.

Ju, D., and Xie, Y. (2004). Proteasomal degradation of RPN4 via two distinct mechanisms, ubiquitin-dependent and -independent. J. Biol. Chem. *279*, 23851–23854.

Kim, Y.C., and DeMartino, G.N. (2011). C termini of proteasomal ATPases play nonequivalent roles in cellular assembly of mammalian 26 S proteasome. J. Biol. Chem. *286*, 26652–26666.

Kim, Y.C., Li, X., Thompson, D., and DeMartino, G.N. (2013). ATP binding by proteasomal ATPases regulates cellular assembly and substrate-induced functions of the 26 S proteasome. J. Biol. Chem. *288*, 3334–3345.

Kim, Y.C., Snoberger, A., Schupp, J., and Smith, D.M. (2015). ATP binding to neighbouring subunits and intersubunit allosteric coupling underlie proteasomal ATPase function. Nat. Commun. *6*, 8520.

Kleijnen, M.F., Roelofs, J., Park, S., Hathaway, N.A., Glickman, M., King, R.W., and Finley, D. (2007). Stability of the proteasome can be regulated allosterically through engagement of its proteolytic active sites. Nat. Struct. Mol. Biol. *14*, 1180–1188.

Köhler, A., Cascio, P., Leggett, D.S., Woo, K.M., Goldberg, A.L., and Finley, D. (2001). The axial channel of the proteasome core particle is gated by the Rpt2 ATPase and controls both substrate entry and product release. Mol. Cell *7*, 1143–1152.

Kusmierczyk, A.R., Kunjappu, M.J., Funakoshi, M., and Hochstrasser, M. (2008). A multimeric assembly factor controls the formation of alternative 20S proteasomes. Nat. Struct. Mol. Biol. *15*, 237–244.

Lander, G.C., Estrin, E., Matyskiela, M.E., Bashore, C., Nogales, E., and Martin, A. (2012). Complete subunit architecture of the proteasome regulatory particle. Nature *482*, 186–191.

Lasker, K., Förster, F., Bohn, S., Walzthoeni, T., Villa, E., Unverdorben, P., Beck, F., Aebersold, R., Sali, A., and Baumeister, W. (2012). Molecular architecture of the 26S proteasome holocomplex determined by an integrative approach. Proc. Natl. Acad. Sci. USA *109*, 1380–1387.

Lee, S.H., Moon, J.H., Yoon, S.K., and Yoon, J.B. (2012). Stable incorporation of ATPase subunits into 19 S regulatory particle of human proteasome requires nucleotide binding and C-terminal tails. J. Biol. Chem. *287*, 9269–9279.

Lindert, S., and McCammon, J.A. (2015). Improved cryoEM-guided iterative molecular dynamics–Rosetta protein structure refinement protocol for high precision protein structure prediction. J. Chem. Theory Comput. *11*, 1337–1346.

Lu, Y., Lee, B.H., King, R.W., Finley, D., and Kirschner, M.W. (2015). Substrate degradation by the proteasome: a single-molecule kinetic analysis. Science *348*, 1250834.

Martin, A., Baker, T.A., and Sauer, R.T. (2008). Pore loops of the AAA+ ClpX machine grip substrates to drive translocation and unfolding. Nat. Struct. Mol. Biol. *15*, 1147–1151.

Mastronarde, D.N. (2005). Automated electron microscope tomography using robust prediction of specimen movements. J. Struct. Biol. *152*, 36–51.

Matyskiela, M.E., Lander, G.C., and Martin, A. (2013). Conformational switching of the 26S proteasome enables substrate degradation. Nat. Struct. Mol. Biol. *20*, 781–788.

Monroe, N., Han, H., Shen, P.S., Sundquist, W.I., and Hill, C.P. (2017). Structural basis of protein translocation by the Vps4-Vta1 AAA ATPase. eLife *6*, e24487.

Nemec, A.A., Howell, L.A., Peterson, A.K., Murray, M.A., and Tomko, R.J., Jr. (2017). Autophagic clearance of proteasomes in yeast requires the conserved sorting nexin Snx4. J. Biol. Chem. *292*, 21466–21480.

Nickell, S., Forster, F., Linaroudis, A., Net, W.D., Beck, F., Hegerl, R., Baumeister, W., and Plitzko, J.M. (2005). TOM software toolbox: acquisition and analysis for electron tomography. J. Struct. Biol. *149*, 227–234.

Nyquist, K., and Martin, A. (2014). Marching to the beat of the ring: polypeptide translocation by AAA+ proteases. Trends Biochem. Sci. *39*, 53–60.

Park, S., Roelofs, J., Kim, W., Robert, J., Schmidt, M., Gygi, S.P., and Finley, D. (2009). Hexameric assembly of the proteasomal ATPases is templated through their C termini. Nature *459*, 866–870.

Park, S., Kim, W., Tian, G., Gygi, S.P., and Finley, D. (2011). Structural defects in the regulatory particle-core particle interface of the proteasome induce a novel proteasome stress response. J. Biol. Chem. *286*, 36652–36666.

Park, S., Li, X., Kim, H.M., Singh, C.R., Tian, G., Hoyt, M.A., Lovell, S., Battaile, K.P., Zolkiewski, M., Coffino, P., et al. (2013). Reconfiguration of the proteasome during chaperone-mediated assembly. Nature *497*, 512–516.

Pettersen, E.F., Goddard, T.D., Huang, C.C., Couch, G.S., Greenblatt, D.M., Meng, E.C., and Ferrin, T.E. (2004). UCSF Chimera–a visualization system for exploratory research and analysis. J. Comput. Chem. *25*, 1605–1612.

Phillips, J.C., Braun, R., Wang, W., Gumbart, J., Tajkhorshid, E., Villa, E., Chipot, C., Skeel, R.D., Kale, L., and Schulten, K. (2005). Scalable molecular dynamics with NAMD. J. Comput. Chem. *26*, 1781–1802.

Puchades, C., Rampello, A.J., Shin, M., Giuliano, C.J., Wiseman, R.L., Glynn, S.E., and Lander, G.C. (2017). Structure of the mitochondrial inner membrane AAA+ protease YME1 gives insight into substrate processing. Science *358*, eaao0464.

Rabl, J., Smith, D.M., Yu, Y., Chang, S.C., Goldberg, A.L., and Cheng, Y. (2008). Mechanism of gate opening in the 20S proteasome by the proteasomal ATPases. Mol. Cell *30*, 360–368.

Ribeiro, J.V., Bernardi, R.C., Rudack, T., Stone, J.E., Phillips, J.C., Freddolino, P.L., and Schulten, K. (2016). QwikMD - integrative molecular dynamics toolkit for novices and experts. Sci. Rep. *6*, 26536.

Rohou, A., and Grigorieff, N. (2015). CTFFIND4: Fast and accurate defocus estimation from electron micrographs. J. Struct. Biol. *192*, 216–221.

Rubin, D.M., Glickman, M.H., Larsen, C.N., Dhruvakumar, S., and Finley, D. (1998). Active site mutants in the six regulatory particle ATPases reveal multiple roles for ATP in the proteasome. EMBO J. *17*, 4909–4919.

Sadre-Bazzaz, K., Whitby, F.G., Robinson, H., Formosa, T., and Hill, C.P. (2010). Structure of a Blm10 complex reveals common mechanisms for proteasome binding and gate opening. Mol. Cell *37*, 728–735.

Saeki, Y., Isono, E., and Toh, E.A. (2005). Preparation of ubiquitinated substrates by the PY motif-insertion method for monitoring 26S proteasome activity. Methods Enzymol. *399*, 215–227.

Scheres, S.H. (2012). RELION: implementation of a Bayesian approach to cryo-EM structure determination. J. Struct. Biol. *180*, 519–530.

Schmidt, M., and Finley, D. (2014). Regulation of proteasome activity in health and disease. Biochim. Biophys. Acta *1843*, 13–25.

Schweitzer, A., Aufderheide, A., Rudack, T., Beck, F., Pfeifer, G., Plitzko, J.M., Sakata, E., Schulten, K., Förster, F., and Baumeister, W. (2016). Structure of the human 26S proteasome at a resolution of 3.9 Å. Proc. Natl. Acad. Sci. USA *113*, 7816–7821.

Śledź, P., Unverdorben, P., Beck, F., Pfeifer, G., Schweitzer, A., Förster, F., and Baumeister, W. (2013). Structure of the 26S proteasome with ATP-γS bound provides insights into the mechanism of nucleotide-dependent substrate translocation. Proc. Natl. Acad. Sci. USA *110*, 7264–7269.

Smith, D.M., Chang, S.C., Park, S., Finley, D., Cheng, Y., and Goldberg, A.L. (2007). Docking of the proteasomal ATPases' carboxyl termini in the 20S proteasome's alpha ring opens the gate for substrate entry. Mol. Cell *27*, 731–744.

Smith, D.M., Fraga, H., Reis, C., Kafri, G., and Goldberg, A.L. (2011). ATP binds to proteasomal ATPases in pairs with distinct functional effects, implying an ordered reaction cycle. Cell *144*, 526–538.

Song, Y., DiMaio, F., Wang, R.Y., Kim, D., Miles, C., Brunette, T., Thompson, J., and Baker, D. (2013). High-resolution comparative modeling with RosettaCM. Structure *21*, 1735–1742.

Tomko, R.J., Jr., and Hochstrasser, M. (2013). Molecular architecture and assembly of the eukaryotic proteasome. Annu. Rev. Biochem. *82*, 415–445.

Tomko, R.J., Jr., Funakoshi, M., Schneider, K., Wang, J., and Hochstrasser, M. (2010). Heterohexameric ring arrangement of the eukaryotic proteasomal

ATPases: implications for proteasome structure and assembly. Mol. Cell *38*, 393–403.

Tomko, R.J., Jr., Taylor, D.W., Chen, Z.A., Wang, H.W., Rappsilber, J., and Hochstrasser, M. (2015). A single α helix drives extensive remodeling of the proteasome lid and completion of regulatory particle assembly. Cell *163*, 432–444.

Trabuco, L.G., Villa, E., Schreiner, E., Harrison, C.B., and Schulten, K. (2009). Molecular dynamics flexible fitting: a practical guide to combine cryo-electron microscopy and X-ray crystallography. Methods *49*, 174–180.

Unverdorben, P., Beck, F., Śledź, P., Schweitzer, A., Pfeifer, G., Plitzko, J.M., Baumeister, W., and Förster, F. (2014). Deep classification of a large cryo-EM dataset defines the conformational landscape of the 26S proteasome. Proc. Natl. Acad. Sci. USA *111*, 5544–5549.

Voges, D., Zwickl, P., and Baumeister, W. (1999). The 26S proteasome: a molecular machine designed for controlled proteolysis. Annu. Rev. Biochem. *68*, 1015–1068.

Wehmer, M., and Sakata, E. (2016). Recent advances in the structural biology of the 26S proteasome. Int. J. Biochem. Cell Biol. *79*, 437–442.

Wehmer, M., Rudack, T., Beck, F., Aufderheide, A., Pfeifer, G., Plitzko, J.M., Förster, F., Schulten, K., Baumeister, W., and Sakata, E. (2017). Structural insights into the functional cycle of the ATPase module of the 26S proteasome. Proc. Natl. Acad. Sci. USA *114*, 1305–1310.

Whitby, F.G., Masters, E.I., Kramer, L., Knowlton, J.R., Yao, Y., Wang, C.C., and Hill, C.P. (2000). Structural basis for the activation of 20S proteasomes by 11S regulators. Nature *408*, 115–120.

Xie, Y., and Varshavsky, A. (2001). RPN4 is a ligand, substrate, and transcriptional regulator of the 26S proteasome: a negative feedback circuit. Proc. Natl. Acad. Sci. USA *98*, 3056–3061.

Yu, Y., Smith, D.M., Kim, H.M., Rodriguez, V., Goldberg, A.L., and Cheng, Y. (2010). Interactions of PAN's C-termini with archaeal 20S proteasome and implications for the eukaryotic proteasome-ATPase interactions. EMBO J. *29*, 692–702.

Zheng, S.Q., Palovcak, E., Armache, J.P., Verba, K.A., Cheng, Y., and Agard, D.A. (2017). MotionCor2: anisotropic correction of beam-induced motion for improved cryo-electron microscopy. Nat. Methods *14*, 331–332.

STAR★METHODS

KEY RESOURCES TABLE

REAGENT or RESOURCE	SOURCE	IDENTIFIER
Antibodies		
Anti-Rpt1	Geng and Tansey, 2012	Clone 19S-2
Anti-Rpt2	Enzo Life Sciences	Cat# PW8160; RRID: AB_10541229
Anti-Rpt5	Enzo Life Sciences	Cat# PW8245; RRID: AB_10555018
Anti-Rpn12	This study	N/A
Anti-20S	Enzo Life Sciences	Cat# PW9355; RRID: AB_2052400
Anti-V5	Life Technologies	Cat# 46-0705; RRID: AB_2556564
Anti-HA	BioLegend	Cat# 901502; RRID: AB_2565007
Anti-ubiquitin	Santa Cruz Biotech	Cat# sc-8017; RRID: AB_628423
Anti-glucose-6-phosphate-dehydrogenase (G6PD)	Sigma Aldrich	Cat# A9521-1VL; RRID: AB_258454
Bacterial and Virus Strains		
TOP10 F'	Life Technologies	Cat #C303003
BL21-STAR (DE3)	EMD Millipore	Cat #71400-3
Chemicals, Peptides, and Recombinant Proteins		
Suc-LLVY-AMC	R&D Systems	Cat# S28005M
Adenosine triphosphate (ATP)	Sigma-Aldrich	Cat# A2383
Adenosine 5′-[γ-thio]triphosphate (ATPγS)	Enzo Life Sciences	Cat# ALX-480-066- M005
Adenylyl-imidodiphosphate (AMP-PNP)	Sigma-Aldrich	Cat# A2647
3X FLAG® Peptide	Sigma-Aldrich	Cat# F4799
ANTI-FLAG® M2 Affinity Agarose Gel	Sigma-Aldrich	Cat# A2220
Creatine phosphokinase	Sigma-Aldrich	Cat# CK-RO Roche
Creatine phosphate, disodium salt	Sigma-Aldrich	Cat# 2380 EMD MILLIPORE
Deposited Data		
Cryo-EM model of the *S. cerevisiae* 26S proteasome, s1 state	This study	PDB: 6FVT
Cryo-EM map of the *S. cerevisiae* 26S proteasome, s1 state	Wehmer et al., 2017	EMDB: 3534
Cryo-EM model of the S. cerevisiae 26S proteasome, s2 state	This study	PDB: 6FVU
Cryo-EM map of the S. cerevisiae 26S proteasome, s2 state	Wehmer et al., 2017	EMDB: 3535
Cryo-EM model of the S. cerevisiae 26S proteasome, s3 state	This study	PDB: 6FVV
Cryo-EM map of the S. cerevisiae 26S proteasome, s3 state	This study	EMDB: 4321
Cryo-EM model of the S. cerevisiae 26S proteasome, s4 state)	This study	PDB: 6FVW
Cryo-EM map of the S. cerevisiae 26S proteasome, s4 state	This study	EMDB: 4322
Cryo-EM model of the S. cerevisiae 26S proteasome, s5 state	This study	PDB: 6FVX
Cryo-EM map of the S. cerevisiae 26S proteasome, s5 state	This study	EMDB: 4323
Cryo-EM model of the S. cerevisiae 26S proteasome, s6 state	This study	PDB: 6FVY
Cryo-EM map of the S. cerevisiae 26S proteasome, s6 state	This study	EMDB: 4324

(*Continued on next page*)

Continued

REAGENT or RESOURCE	SOURCE	IDENTIFIER
Experimental Models: Organisms/Strains		
S. cerevisiae strain RTY1 (aka MHY500)	Chen et al., 1993	N/A
For isogenic mutants of RTY1 used herein, see Table S1.	This study	N/A
S. cerevisiae strain YYS40	Saeki et al., 2005	N/A
Recombinant DNA		
For plasmids used herein, see Table S2.	This study	N/A
Software and Algorithms		
Prism 7	GraphPad	https://www.graphpad.com/scientific-software/prism/
Image Lab	Bio-Rad	http://www.bio-rad.com/en-ch/product/image-lab-software?ID=KRE6P5E8Z
Latitude S Software	Gatan	http://www.gatan.com/products/tem-imaging-spectroscopy/latitude-s-software
SerialEM	Mastronarde, 2005	http://bio3d.colorado.edu/SerialEM/
RELION	Scheres, 2012	http://www2.mrc-lmb.cam.ac.uk/relion/index.php/Main_Page
UCSF CHIMERA	Pettersen et al., 2004	http://www.cgl.ucsf.edu/chimera
MATLAB	MathWorks	https://www.mathworks.com/
VMD	Humphrey et al., 1996	http://www.ks.uiuc.edu/Research/vmd/
QwikMD	Ribeiro et al., 2016	http://www.ks.uiuc.edu/Research/qwikmd/
NAMD	Phillips et al., 2005	http://www.ks.uiuc.edu/Research/namd/
TOM toolbox	Nickell et al., 2005	https://www.biochem.mpg.de/tom
Rosetta	Song et al, 2013	https://www.rosettacommons.org/software

CONTACT FOR REAGENT AND RESOURCE SHARING

Further information and requests for resources and reagents should be directed to and will be fulfilled by Robert J. Tomko Jr. (robert.tomko@med.fsu.edu).

EXPERIMENTAL MODEL AND SUBJECT DETAILS

Yeast strains and media

All yeast strains were grown in YPD medium at 30°C, except for *RPT* Walker B mutants and their respective controls, which were grown at 25°C. When selection for a plasmid was necessary, strains were grown in synthetic dropout medium lacking the appropriate auxotrophic agent at 30°C or 25°C as above. Yeast manipulations were carried out according to standard protocols (Guthrie and Fink, 1991). To evaluate the impact of CP gate and pore residues, we created a set of strains with chromosomal deletions of each alpha subunit gene covered by a *URA3*-marked plasmid bearing the corresponding WT allele. Single mutant strains were crossed, and double mutants were isolated after sporulation and dissection. Double mutants were identified via growth on selective media and/or colony PCR. WT or mutant alpha subunit alleles on *LEU2*- or *TRP1*-marked plasmids were then introduced into the double mutant strain, and the *URA3*-marked plasmids were evicted by selection on 5-fluoro-orotic acid media. For growth assays, the indicated strains were spotted as six-fold serial dilutions in water onto the indicated media. Cadmium plates were poured fresh and dried for one hour in a laminar flow hood immediately before use. Yeast strains used in this study are listed in Table S1.

Plasmids

All plasmids were constructed using standard molecular cloning techniques using TOP10 F' as a host strain and were verified by DNA sequencing prior to use. Plasmids used in this study are listed in Table S2. Complete sequences and construction details are available upon request.

METHOD DETAILS

Disulfide Crosslinking of Conformation-specific Proteasome Reporters

Crosslinking of lid and base subunits was performed essentially as described previously for the Rpt subunits (Tomko et al., 2010) with some modification. Yeast expressing proteins with the desired cysteine substitutions were grown to mid-log phase, and 20

OD_{600} equivalents were harvested and converted to spheroplasts. These were lysed in 150 μL of ice-cold lysis buffer (50mM HEPES, pH 7.5, 150mM NaCl, 5mM $MgCl_2$) containing 2mM (or the indicated concentration) of the appropriate nucleotide (ATP, ATPγS, or AMP-PNP). The cells were lysed by vortexing three times at top speed for 30 s with 1 min intervals on ice in between. The lysates were centrifuged at 21,000 x g at 4°C for 10 min. The protein content of supernatants was normalized with lysis buffer containing the appropriate nucleotide. Crosslinking was initiated with 250μM $CuCl_2$ at 25°C. After 10 minutes, 2.5 μL of 20x stop buffer (200 mM *N*-ethylmaleimide) and EDTA were added. For reduction of engineered disulfides prior to SDS-PAGE analysis, 2 μL of 1 M DTT, pH 7.0 was added to the sample for ten minutes at room temperature before electrophoresis. Samples were boiled in non-reducing Laemmli buffer, loaded onto 10% SDS-PAGE gels, and separated by electrophoresis at 200 V.

Native polyacrylamide gel electrophoresis

Cell extracts (50-100 μg total protein) were separated by non-denaturing polyacrylamide electrophoresis exactly as described previously (Nemec et al., 2017). Specifically, cells were grown to OD_{600} ≈1.5 - 2.0, harvested by centrifugation at 5,000 x g for five minutes at RT, followed by washing in 25 mL of ice-cold dH_2O. Cells were centrifuged again at 5,000 x g for two minutes, 4°C, and the supernatant was decanted. Cell pellets were then frozen in liquid nitrogen and ground into powder in a mortar and pestle. Cell powder was hydrated in one powder volume of Extraction Buffer (50 mM Tris-Cl, pH 7.5, 5 mM $MgCl_2$, 10% glycerol, 1 mM ATP, 0.015% w/v xylene cyanol), and incubated with frequent vortexing for 10 minutes on ice. Cell debris was removed by centrifugation at 21,000 x g for 10 minutes at 4°C. Supernatants containing equal amounts of protein (determined by BCA assay) were loaded onto 4% native polyacrylamide gels cast with 0.5 mM ATP and with a 3.5% polyacrylamide stacker containing 2.5% sucrose and 0.5 mM ATP. Samples were electrophoresed at 100 V, 4°C until the dye front escaped (typically 3 - 3.5 hours).

Measurement of peptidase activity

For measurement of suc-LLVY-AMC hydrolysis in non-denaturing gels, 100 μg of cell extract was separated as described above. The gel was then incubated in Overlay buffer (50 mM Tris-Cl, pH 7.5, 5 mM $MgCl_2$, 10% glycerol, 1 mM ATP) containing 50 μM suc-LLVY-AMC for 30 minutes at 30°C with occasional gentle agitation. Liberated AMC was detected in a Bio-Rad Chemi-doc MP imaging system with the pre-programmed excitation and emission settings for ethidium bromide. To normalize peptidase activity between samples, an equal amount of the cell extracts used for the peptidase assay was separated by native PAGE and subjected to anti-Rpt1 immunoblotting as described below. The AMC fluorescence intensity was then divided by the intensity of the Rpt1 signal to normalize between samples with slightly different proteasome abundances.

Analysis of suc-LLVY-AMC hydrolysis by purified WT or Walker B mutant proteasomes was conducted in 384-well black microplates on a Biotek Synergy H1MF. Proteasomes (10 nM RP_2CP) were incubated with 50 μM suc-LLVY-AMC in 26S Buffer with ATP-regenerating system (50 mM HEPES-OH, pH 7.5, 50 mM NaCl, 50 mM KCl, 5 mM $MgCl_2$, 10% glycerol, 0.5 mM ATP, 60 μg/mL creatine kinase, and 16 mM creatine phosphate) and fluorescence from liberated AMC (Ex360, Em460) was monitored for 900 s. Relative rates were determined from the initial slopes of fluorescence versus time.

Production of anti-Rpn12 antisera

BL21-STAR(DE3) *E. coli* transformed with pRT1122 (Tomko et al., 2015) were grown in 4 L of LB containing 40 μg/mL kanamycin at 37°C. Once the culture reached OD_{600} ≈0.6, IPTG was added to 0.5 mM and the temperature was lowered to 16°C. Induction was allowed to occur for approx. 18 hours, at which time the cells were harvested by centrifugation at 10,000 x g for 5 minutes at 25°C. The pellet was resuspended in Lid Buffer (50 mM HEPES-OH, pH 7.5, 100 mM NaCl, 100 mM KCl, 5% glycerol) containing 20 mM imidazole, and cells were lysed using a Microfluidics Corp. Microfluidizer M-100EH. Lysates were cleared by centrifugation for 20 min at 30,000 x *g* at 4°C and bound to 5 mL Ni-NTA resin for 30 minutes at 4°C. The resin was then washed twice in batch mode with 50 mL of Lid Buffer with 20 mM imidazole, followed by a final wash with 50 mL in column mode. Bound Rpn12 was then eluted by the addition of two column volumes of Lid Buffer + 250 mM imidazole. The final 1.5 column volumes was retained, and concentrated to < 2 mL using a 10,000 MWCO filter (Amicon). The concentrated protein was centrifuged at 21,000 x g for one minute to pellet any precipitated material, and the supernatant was loaded onto a Sephacryl S-200 column pre-equilibrated with Lid buffer. Essentially pure fractions were identified via SDS-PAGE, pooled, concentrated to approx. 250 μM, and flash-frozen in liquid nitrogen.

Approximately 10 mg of purified Rpn12 was loaded onto a 10% SDS-PAGE gel with a single large sample well and separated at 200 V until the dye front escaped. The gel was then stained with Gelcode Blue (Thermo), and the band corresponding to recombinant Rpn12 was excised. The polyacrylamide slice was sent to Cocalico Biologicals for antiserum production. The crude antiserum showed no reactivity with any other yeast proteins via immunoblotting of SDS-PAGE or native PAGE-separated extracts, and thus was used without further purification.

Immunoblot Analyses

Denaturing and non-denaturing gels were transferred to PVDF membranes (EMD Millipore) at 100 V for one hour at 4°C. Membranes were probed with antibodies against V5 tag (1:5000), HA (1:10,000), Rpn12 (1:5000), Rpt1 (1:10,000), Rpt2 (1:5000), Rpt5 (1:10,000), 20S CP (1:2500), ubiquitin (1:1000), or G6PD (1:10,000). After probing with HRP-conjugated secondary antibodies and ECL reagent, the blots were imaged using a Bio-Rad ChemiDoc MP. Band intensities were quantified from unsaturated raw image files using

ImageLab software (Bio-Rad). The percentage of crosslinking was determined by dividing the band representing crosslinked subunits by the sum of crosslinked and uncrosslinked subunit for each lane.

Purification of Proteasomes

Purification of endogenous proteasomes from *S. cerevisiae* was performed as described in (Wehmer et al., 2017). In brief, *S. cerevisiae* cells were grown for 48 hours and harvested in stationary phase. The purification of 3XFLAG-tagged 26S proteasome was performed in two steps. The first step was carried out via cell lysis, followed by affinity purification using M2 anti-FLAG beads (Sigma A2220). After incubation for 1.5 h at 4°C the proteasome was eluted with FLAG peptide. An overnight sucrose gradient was carried out for the second purification step. Proteasome-containing fractions were identified by degradation of the peptide suc-LLVY-AMC, SDS-PAGE analysis, Bradford assay (Bradford, 1976) and negative stain electron microscopy. Until further use the samples were stored at −80°C after flash freezing with liquid nitrogen. For purifying ATPγS-containing 26S proteasomes, either 2 mM ATPγS or 4 mM ATPγS, instead of 4 mM ATP, and 16 mM creatine phosphate and 0.03 mg/mL creatine phosphate kinase were added to the sucrose gradient. The sucrose gradient was centrifuged in a Beckman SW41 rotor for 17 h at 4°C at 28000 rpm. The three EQ mutants were purified with buffer A [100 mM Tris·HCl (pH 7.4), 100 mM NaCl, 10% (vol/vol) glycerol, 4 mM $MgCl_2$, 4 mM ATP] and sucrose gradient buffer [15%–30% sucrose (wt/vol), 20 mM HEPES (pH 7.4), 40mM NaCl, 4 mM DTT, 4 mM $MgCl_2$, 4 mM ATP]. The sucrose gradient was centrifuged in a Beckman SW60 rotor for 16 h at 4°C at 29000 rpm.

Data acquisition

Data acquisition was performed with an FEI Titan Krios electron microscope. Proteasome samples were plunge frozen on Lacey carbon-coated grids using a Manual Plunger. Datasets were collected with a K2 camera using the program Latitude software (Gatan, Inc.). Movies were acquired at a pixel size of 1.38 Å. A total dose of ~35 electrons was distributed over 33 frames for the K2 camera. The nominal defocus range of the acquisition varied from 1.8 to 3 μm.

Image processing

All movie frames were aligned translationally and summed with MotionCor2. During frame alignment, recorded movies were subjected to motion correction (Zheng et al., 2017). The contrast transfer function (CTF) was estimated using CTFFIND3 (Rohou and Grigorieff, 2015) and micrographs with a defocus outside the range of 0.8 to 3.5 um and a CTF fit score below 0.05 were discarded. Because of the high number of micrographs from the 2 mM ATPγS and 4 mM ATPγS samples, micrographs with an estimated resolution over 4.5 Å were also discarded.

Single particle analysis

Single particle processing was performed following the procedure described by (Aufderheide et al., 2015; Schweitzer et al., 2016). Briefly, in the first step, 26S proteasomes were picked automatically using the TOM toolbox (Beck et al., 2012). All further single particle analysis steps were performed using the RELION software package (Scheres, 2012). Proteasome particles were extracted using a box size of 384 pixels. After 2D classification, only 2D-classes containing particles with a complete 26S were retained. Each dataset was then reconstructed using a down-filtered 3D reference of the 26S proteasome. Pseudo-single-capped 26S particles (pseudo-sc26S) were generated using the resulting angles of the reconstruction and classified using a soft-edged mask focused on the RP. All previously assigned angles were kept constant during classification. Using the UCSF chimera fit-in map (Pettersen et al., 2004) the previously identified proteasome states s1, s2, s3 and s4 were compared to the 3D class averages (Unverdorben et al., 2014; Wehmer et al., 2017) and classes of the same states were combined for further rounds of classification. When necessary for better comparison each class was first refined with RELION as described below. Classified particles were subjected to several rounds of 3D classification with RELION until the outcome of the resulting classes did not change further. Each state was then refined using a soft-edged mask containing the RP, α-ring and β-ring with a local angular search around the initial angles from the refinement of the polished particles. The resulting density was subjected to post-processing in RELION for resolution determination and B-factor sharpening.

Model Building

Atomic models were generated employing an optimized integrative modeling approach based on the workflow used to obtain the previous structural models of the human (Schweitzer et al., 2016), yeast (Wehmer et al., 2017), and rat (Guo et al., 2018) proteasome. The used modeling approach combines MDFF (Trabuco et al., 2009), Rosetta software, and Monte Carlo backbone and sidechain rotamer search algorithms following the strategy described in Goh et al. (Goh et al., 2016). MDFF simulations were prepared using QwikMD (Ribeiro et al., 2016), analyzed with VMD (Humphrey et al., 1996), and carried out with NAMD. The higher resolution densities of s3 and s4 were used to furnish missing unresolved segments of the previous models of s3 and s4 (Wehmer et al., 2017) and to further refine the model to reflect the higher resolution of the densities. The s5 model was created based on a previous s2 model and the s6 model based on the refined s3 model.

Volume analysis of the nucleotide binding pocket

All Rpt subunits (Rpt1-Rpt6) from models of all states (s1 - s6) were aligned to the interface between Rpt1 and Rpt5 of s1 using Chimera matchmaker. The 36 corresponding EM-maps were aligned accordingly by Chimera matrixcopy and filtered to 7 Å. To focus on the binding pocket, a spherical mask with a diameter of 41 Å was placed around R255 of Rpt1. These preprocessed volumes were hierarchically clustered using MATLAB and TOM-toolbox.

QUANTIFICATION AND STATISTICAL ANALYSIS

Quantification of AMC fluorescence intensity and of band densities was performed on unsaturated images using the Bio-Rad Image Lab software package. Specific replicate numbers (*N*) for each experiment can be found in the corresponding figure legends. In all figures, error bars indicate standard deviations. Statistical significance was addressed in Graphpad Prism 7 by one- or two-way ANOVA with the appropriate post hoc tests as described in the figure legends. Statistical significance was considered $p < 0.05$.

DATA AND SOFTWARE AVAILABILITY

The accession numbers for the single particle reconstructions reported in this paper are EMDB: EMD-4321 (s3), EMD-4322 (s4), EMD-4323 (s5), and EMD-4324 (s6)]. The accession numbers for the atomic coordinates reported in this paper are PDB: 6FVT (s1), 6FVU (s2), 6FVV (s3), 6FVW (s4), 6FVX (s5), and 6FVY (s6).

Cell Reports, Volume *24*

Supplemental Information

Expanded Coverage of the 26S Proteasome Conformational Landscape Reveals Mechanisms of Peptidase Gating

Markus R. Eisele, Randi G. Reed, Till Rudack, Andreas Schweitzer, Florian Beck, Istvan Nagy, Günter Pfeifer, Jürgen M. Plitzko, Wolfgang Baumeister, Robert J. Tomko Jr., and Eri Sakata

Table S1 related to Main Figures 1-7: Yeast strains used in this study.

Name	Genotype
RTY1	*MAT***a** *his3-*Δ*200 leu2-3,112 ura3-52 lys2-801 trp1-1* (alias MHY500)
RTY432	*MAT***a** *his3-*Δ*200 leu2-3,112 ura3-52 lys2-801 trp1-1 RPN5-6xGly-3xFLAG:hphMX4 rpt3Δ::HIS3* [YCplac33-*RPT3*]
RTY1168	*MAT***a** *his3-*Δ*200 leu2-3,112 ura3-52 lys2-801 trp1-1 rpt1Δ::HIS3* [pFL44-*RPT1*]
RTY1171	*MAT***a** *his3-*Δ*200 leu2-3,112 ura3-52 lys2-801 trp1-1 rpt4Δ::HIS3* [YCplac33-*RPT4*]
RTY1173	*MAT***a** *his3-*Δ*200 leu2-3,112 ura3-52 lys2-801 trp1-1 rpt6Δ::HIS3* [YCplac33-*RPT6*]
RTY1179	*MAT*α *his3-*Δ*200 leu2-3,112 ura3-52 lys2-801 trp1-1 rpt6-Δ1:natMX4*
RTY1301	*MAT*α *his3-*Δ*200 leu2-3,112 ura3-52 lys2-801 trp1-1 rpn6Δ::natMX4 rpt6Δ::HIS3* [pRS316-*RPN6*; YCplac33-*RPT6*]
RTY1321	*MAT***a** *his3-*Δ*200 leu2-3,112 ura3-52 lys2-801 trp1-1 rpt2Δ::HIS3* [pRS316-*RPT2*]
RTY1372	*MAT***a** *his3-*Δ*200 leu2-3,112 ura3-52 lys2-801 trp1-1 rpn7Δ::natMX4 rpt2Δ::HIS3* [pRS316-*RPN7*; pRS316-*RPT2*]
RTY1504	*MAT***a** *his3-*Δ*200 leu2-3,112 ura3-52 lys2-801 trp1-1 rpt3Δ::HIS3* [YCplac33-*RPT3*]
RTY1506	*MAT***a** *his3-*Δ*200 leu2-3,112 ura3-52 lys2-801 trp1-1 rpt5Δ::HIS3* [YCplac33-*RPT5*]
RTY1664	*MAT***a** *his3-*Δ*200 leu2-3,112 ura3-52 lys2-801 trp1-1 rpt1-Δ1:kanMX6*
RTY2013	*MAT***a** *his3-*Δ*200 leu2-3,112 ura3-52 lys2-801 trp1-1 RPN5-6xGly-3xFLAG:hphMX4 rpt6Δ::HIS3* [YCplac33-*RPT6*]
RTY2033	*MAT***a** *his3-*Δ*200 leu2-3,112 ura3-52 lys2-801 trp1-1 RPN5-6xGly-3xFLAG:hphMX4 rpt2Δ::HIS3* [pRS316-*RPT2*]
RTY2091	*MAT*α *his3-*Δ*200 leu2-3,112 ura3-52 lys2-801 trp1-1 RPN7(D123C)-6xGly-V5:kanMX6*
RTY2099	*MAT***a** *his3-*Δ*200 leu2-3,112 ura3-52 lys2-801 trp1-1 RPT2(R407C):natMX4*
RTY2112	*MAT***a** *his3-*Δ*200 leu2-3,112 ura3-52 lys2-801 trp1-1 RPN7(D123C)-6xGly-V5:kanMX6 RPT2(R407C):natMX4*
RTY2123	*MAT***a** *his3-*Δ*200 leu2-3,112 ura3-52 lys2-801 trp1-1 rpt1-Δ1:kanMX6 rpt6-Δ1:natMX4*
RTY2166	*MAT***a** *his3-*Δ*200 leu2-3,112 ura3-52 lys2-801 trp1-1 pre8Δ::HIS3 pre9Δ::natMX4* [pRS316-*PRE8*]
RTY2135	*MAT***a** *his3-*Δ*200 leu2-3,112 ura3-52 lys2-801 trp1-1 RPN7(D123C)-6xGly-V5:kanMX6 RPT2(R407C):natMX4 rpt3Δ::HIS3* [YCplac33-*RPT3*]
RTY2137	*MAT***a** *his3-*Δ*200 leu2-3,112 ura3-52 lys2-801 trp1-1 RPN7(D123C)-6xGly-V5:kanMX6 RPT2(R407C):natMX4 rpt6Δ::HIS3* [YCplac33-*RPT6*]
YYS40	*MAT***a** *ade2-1, ura3-1, his3-11, trp1-1, leu2-3,112, can1-100, rpn11::RPN11- 3xFLAG-CYC1term-HIS3*

Table S2 related to Main Figures 1-7: Plasmids used in this study.

Plasmid	Genotype	Source
pRT357	pRS314-*RPT1*	This study
pRT364	YCplac111-*RPT3*	This study
pRT702	YCplac111-*RPT2*	This study
pRT1122	pET42b-6His-Cys-rpn12(C23S,D265A)	(Tomko et al., 2015)
pRT1408	pRS315-*RPT5*	This study
pRT1409	pRS314-*rpt1(E310Q)*	This study
pRT1410	YCplac111-*rpt2(E283Q*)	This study
pRT1411	YCplac111-*rpt3(E273Q*)	This study
pRT1413	pRS315-*rpt5(E282Q*)	This study
pRT1425	pRS314-HA-*RPN6*	This study
pRT1496	YCplac111-*RPT6*	This study
pRT1497	YCplac111-*rpt6(E249Q*)	This study
pRT1528	YCplac111-*RPT4*	This study
pRT1529	YCplac111-*rpt4(E283Q)*	This study
pRT1780	pRS314-HA-*RPN6(T203C)*	This study
pRT1783	YCplac111-*RPT2(R407C)*	This study
pRT1784	YCplac111-*RPT6(G387C)*	This study
pRT1834	YCplac111-*rpt2(E283Q, R407C)*	This study
pES1	pET28a-5Ub-DHFR-UR-His	This study

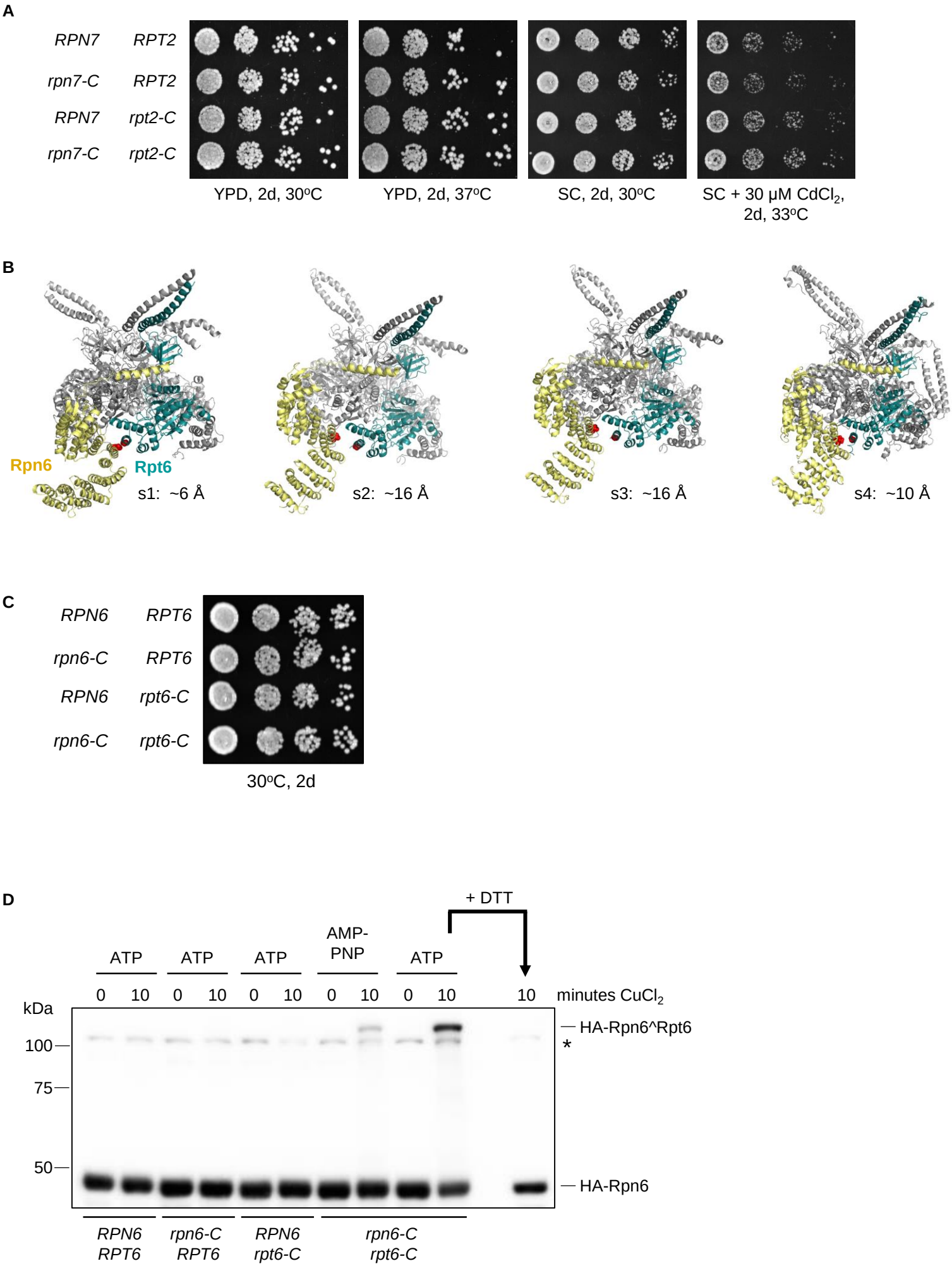
A
RPN7 RPT2
rpn7-C RPT2
RPN7 rpt2-C
rpn7-C rpt2-C
YPD, 2d, 30ºC
YPD, 2d, 37ºC
SC, 2d, 30ºC
SC + 30 µM CdCl2, 2d, 33ºC
B
Rpn6
Rpt6
s1: ~6 Å
s2: ~16 Å
s3: ~16 Å
s4: ~10 Å
C
RPN6 RPT6
rpn6-C RPT6
RPN6 rpt6-C
rpn6-C rpt6-C
30ºC, 2d
D
+ DTT
ATP
ATP
ATP
AMP-PNP
ATP
0 10 0 10 0 10 0 10 0 10 10
minutes CuCl2
kDa
100
75
50
HA-Rpn6^Rpt6
*
HA-Rpn6
RPN6 RPT6
rpn6-C RPT6
RPN6 rpt6-C
rpn6-C rpt6-C

Figure S1

Figure S1 related to Figure 1. *A,* Cysteine substitutions do not impact cell health. The strains shown were plated as serial dilutions on YPD, SC, or SC+ 30 μM $CdCl_2$ plates and incubated at the temperatures shown. *B*, Rpn6-T203 and Rpt6-G387 serve as an alternative conformational reporter. Rpn6 is shown in gold, Rpt6 in blue, and the other five Rpt subunits are shown in grey. All other subunits are omitted for clarity. The T203 and G387C residues are shown as red spheres, and the distances between their α carbons is listed in Angstroms. *C*, No obvious growth impairment in cells harboring the T203C and G387C substitutions. Serial dilutions were performed as in (*A*) above. *D*, Disulfide crosslinking of Rpn6 and Rpt6 is dependent upon engineered cysteines and impacted by nucleotide. Crosslinking was induced in whole cell extracts (WCE) prepared in the presence of 2 mM of the indicated nucleotide with $CuCl_2$ for ten minutes. Proteins were resolved by non-denaturing SDS-PAGE and examined by anti-HA (Rpn6) immunoblotting. For the last lane, the WCE was incubated with 10 mM DTT for 10 minutes prior to gel loading.

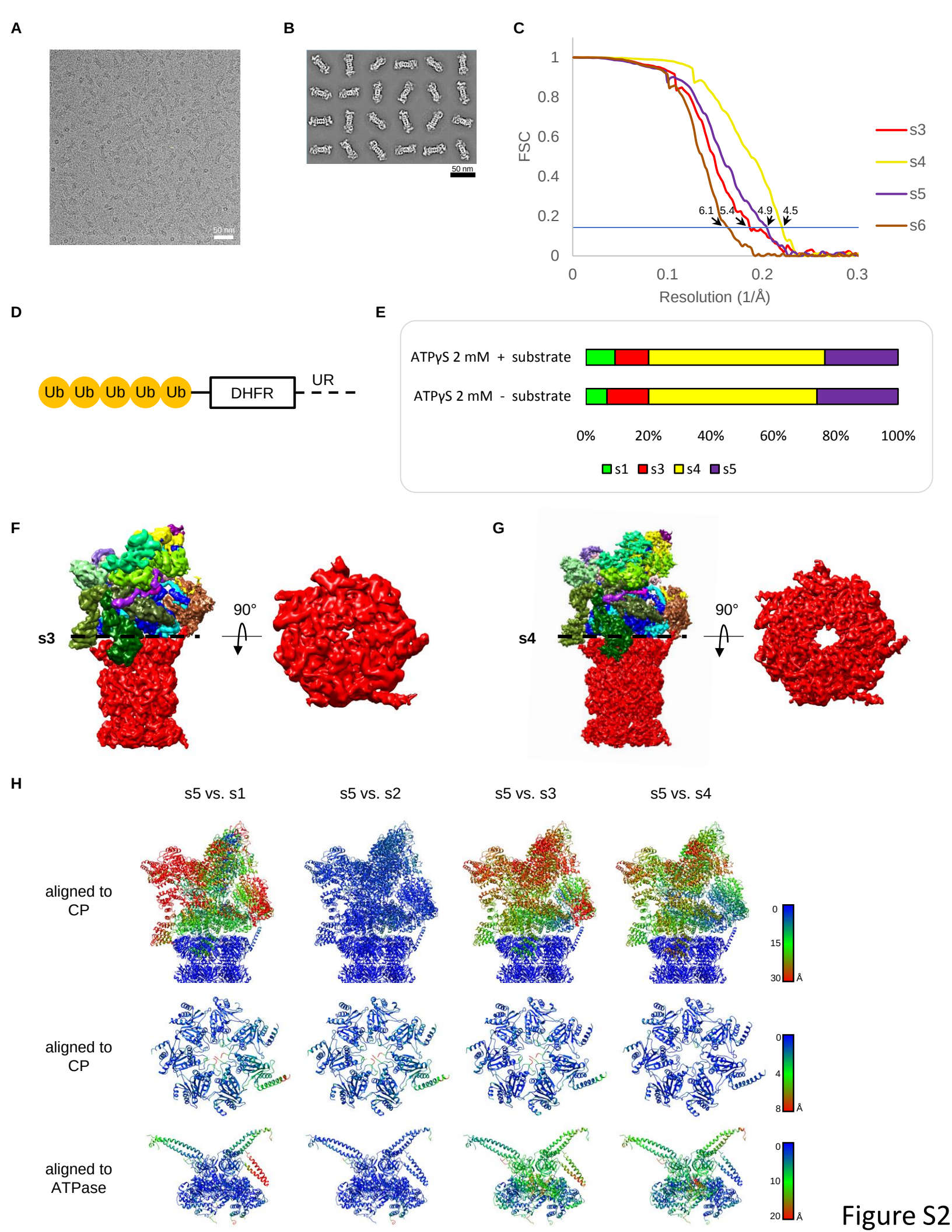
A
50 nm
B
50 nm
C
FSC
Resolution (1/Å)
6.1
5.4
4.9
4.5
s3
s4
s5
s6
D
Ub
Ub
Ub
Ub
Ub
DHFR
UR
E
ATPγS 2 mM + substrate
ATPγS 2 mM - substrate
0%
20%
40%
60%
80%
100%
s1
s3
s4
s5
F
s3
90°
G
s4
90°
H
s5 vs. s1
s5 vs. s2
s5 vs. s3
s5 vs. s4
aligned to CP
aligned to CP
aligned to ATPase
Å

Figure S2

Figure S2 related to Figure 2. *A*, Double capped particles are predominantly visible on a typical micrograph. *B*, Particles were 2D sorted and only suitable reference-free 2D class averages were used for further 3D analysis. *C*, Combined particles of each state resulted in a resolution of 4.5 Å for s4, 4.9 Å for s5, 5.4 Å for s3 and 6.1 Å for s6 on the basis of the gold-standard FSC criterion ($FSC_{0.143}$). *D*, Schematic of linear ubiquitinated DHFR with an unstructured region at the C-terminus. *E*, State distribution of classified 2 mM ATPγS data set with and without model substrate. *F* and *G*, Cryo-EM reconstruction of classified s3 particles (F) and s4 particles (G). The 26S proteasome is colored according to Fig 2B. A clear density is visible in the center of the 20S in the s3 state and no density is visible in the s4 state. *H*, Residue-wise RMSD of the whole 26S proteasome, the 20S gate and the AAA+ ATPase (in Å) between the s5 vs. s1 state (left), s5 vs. s2 state, s5 vs. s3 state and s5 vs. s4 state, aligned to the CP or to the ATPase. For the gate RMSD plots, the compared structures (either s1, s2, s3 or s4) are shown. In all other panels, the measured RMSD is plotted on the s5 structure.

A

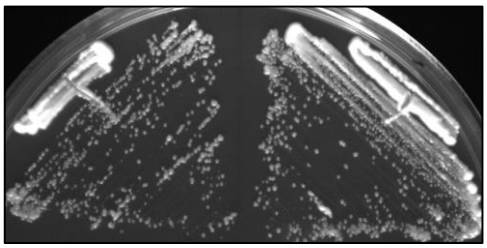

YPD, 2d, 37°C

B

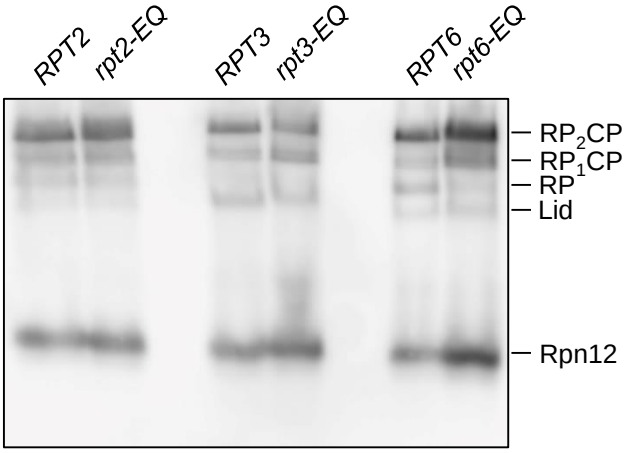

Anti-Rpn12 (lid) blot

C

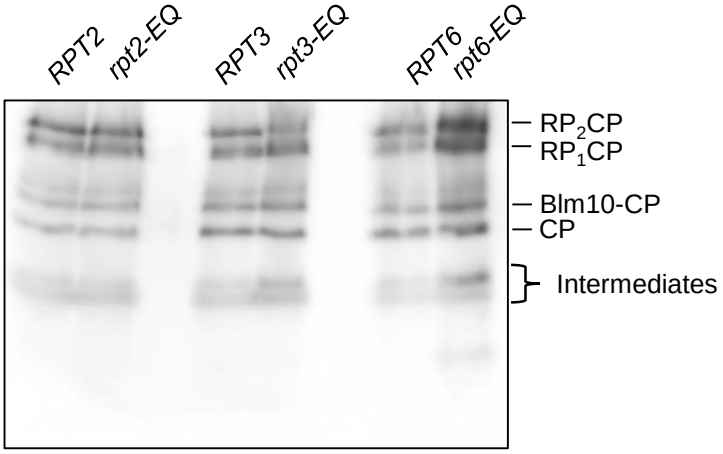

Anti-20S (CP) blot

Figure S3

Figure S3 related to Figure 3. *A*, No evidence of temperature sensitivity in *rpt2-EQ* yeast. WT or *rpt2-EQ* yeast were struck on YPD, and incubated at 37ºC for two days. *B* and *C*, Native gel immunoblot analysis of the indicated strains with anti-Rpn12 (*B*) or anti-20S (*C*) antibodies reveal no obvious structural defects. CP assembly intermediates are indicated with a bracket.

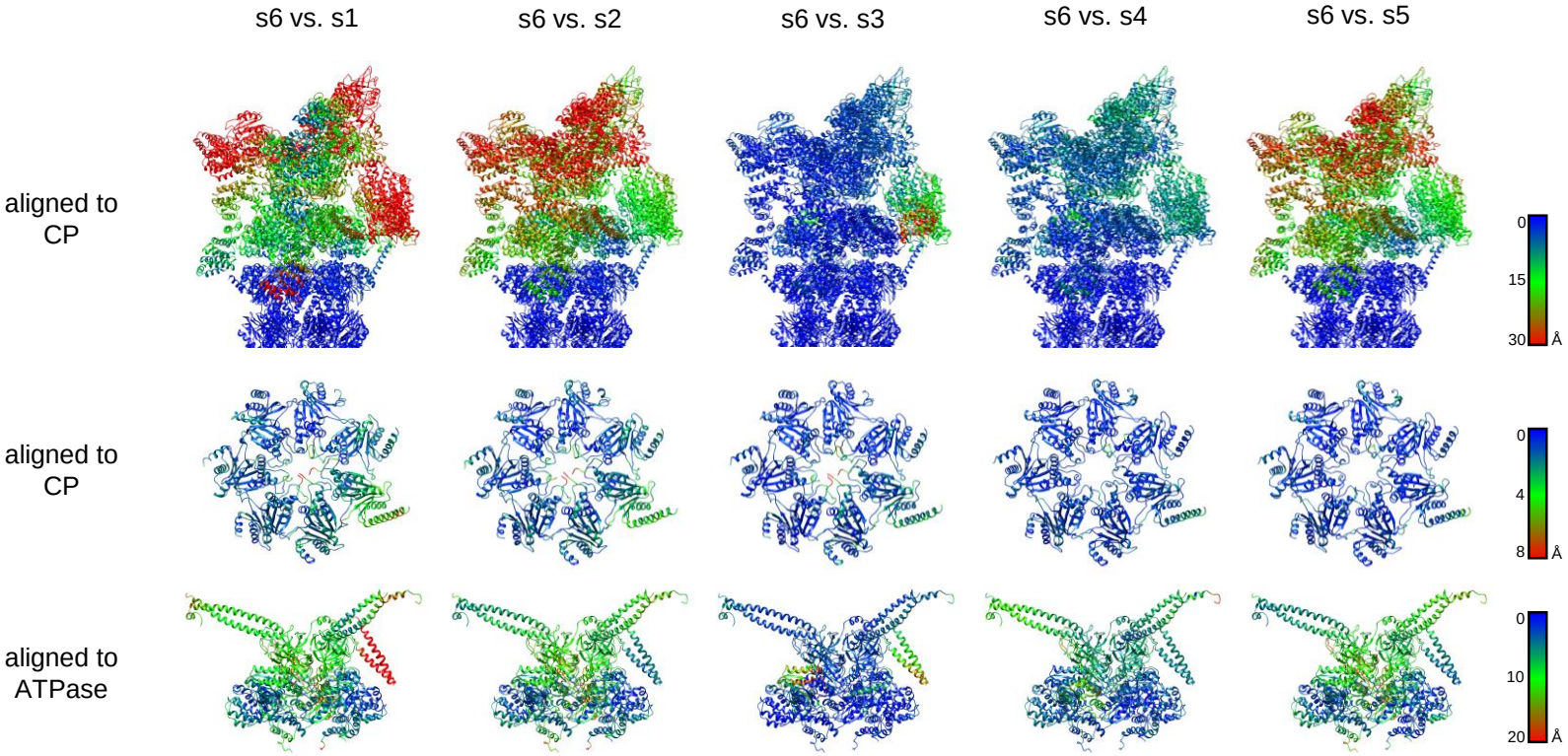
s6 vs. s1
s6 vs. s2
s6 vs. s3
s6 vs. s4
s6 vs. s5
aligned to CP
aligned to CP
aligned to ATPase
0
15
30
Å
0
4
8
Å
0
10
20
Å

Figure S4

Figure S4 related to Figure 4. Residue-wise RMSD of the whole 26S proteasome, the 20S gate and the AAA+ ATPase (in Å) between the s6 vs. s1 state (left), s6 vs. s2 state, s6 vs. s3 state, s6 vs. s4 state and s6 vs. s5 state, aligned to the CP or to the ATPase. For the gate RMSD plots, the compared structures (either s1, s2, s3, s4 or s5) are shown. In all other panels, the RMSD is plotted on the s6 structure.

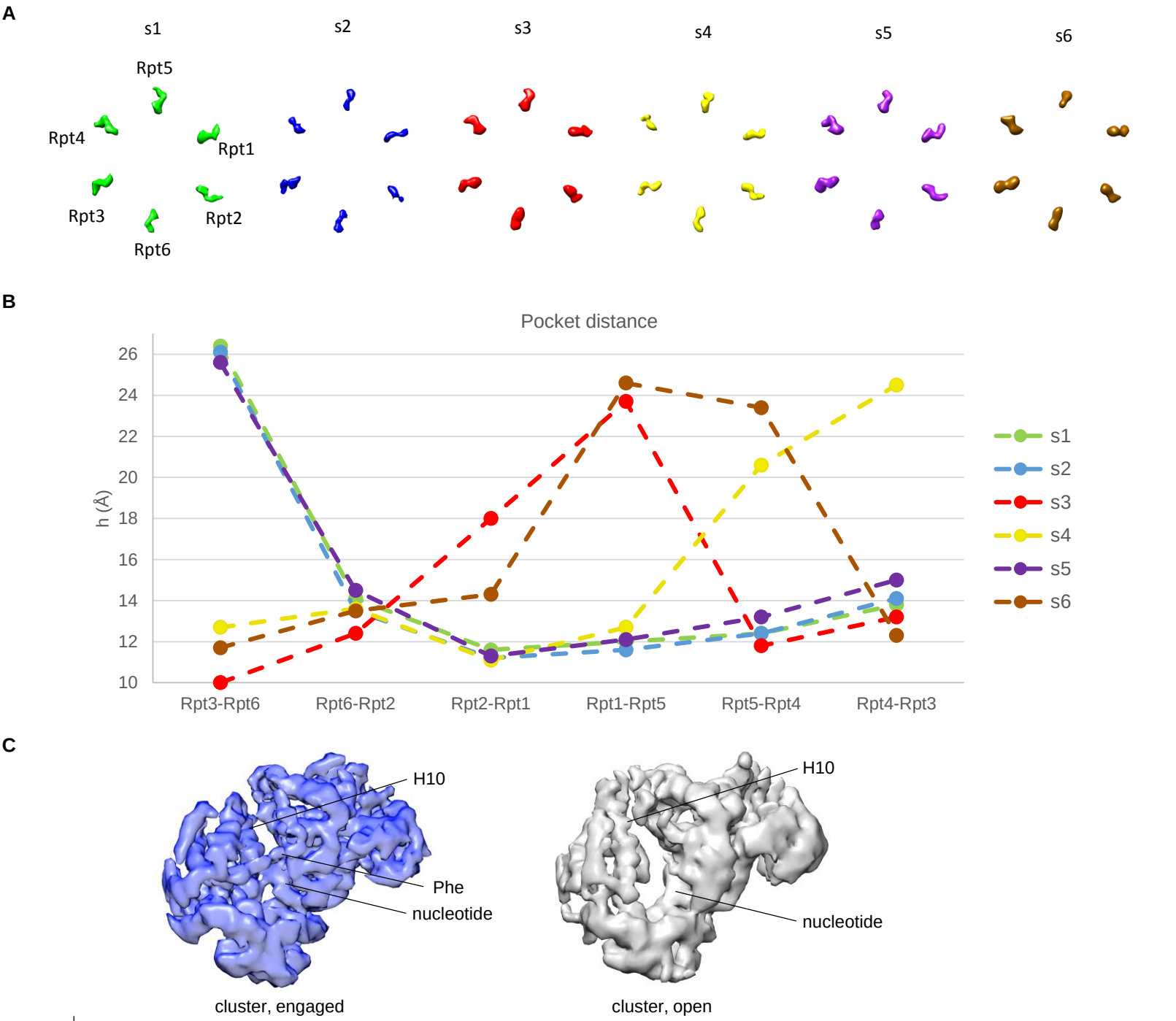

	s1	s2	s5	s3	s6	s4
Rpt3-Rpt6	27	28	29	22	25	23
Rpt6-Rpt2	3	1	2	16	18	21
Rpt2-Rpt1	4	7	5	32	35	12
Rpt1-Rpt5	6	15	24	30	36	13
Rpt5-Rpt4	8	11	9	10	34	33
Rpt4-Rpt3	19	20	14	17	26	31

Figure S5

Figure S5 related to Figure 5. *A,* Comparison of nucleotide bound states in all six states. A simulated map of the AAA+ ring model without nucleotides was subtracted from the experimental map. EMD-3534 and EMD-3535 were used for s1 and s2 (Wehmer et al., 2017). The difference maps always show six nucleotides for each state. *B,* The state of the pocket is determined by measuring the distance between the end of the H10 helix of one Rpt subunit and the tip of H6 helix of the adjacent clockwise subunit. Color coding of each state would corresponds to the one in Figure 6A. *C,* Assessment of the EM density of the nucleotide binding pocket. Volumes of all Rpt subunits interfaces were aligned and hierarchically clustered by their similarity. The aligned densities were divided into two large clusters; the average of the blue class is assigned to the engaged conformation whereas the gray is assigned to the open conformation. An overview of the clustering results of the Rpt interface is shown in right lower panel. The numbers in the columns correspond to the numbering of the clustering on the left.

A

Rpt6 – C-terminus

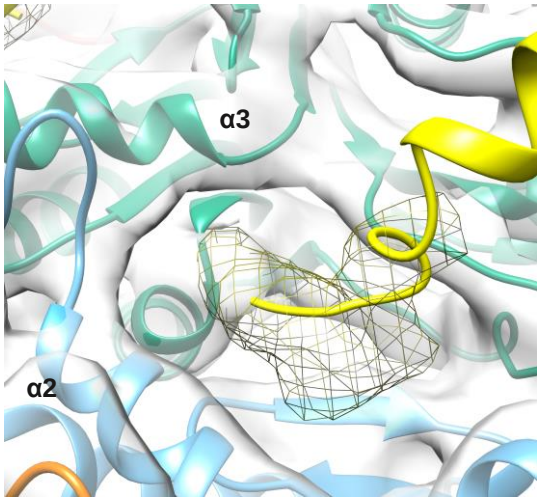

Rpt1 – C-terminus

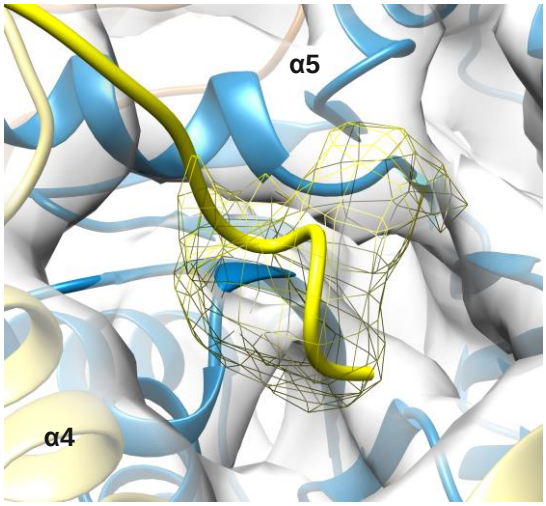

B

hsRpt1	406	EKDFLEAVNKVIKSYAKFSATPRYMTYN
mmRpt1	448	EKDFLEAVNKVIKSYAKFSATPRYMTYN
drRpt1	406	EKDFLEAVNKVIKSYAKFSATPRYMTYN
xlRpt1	406	EKDFLEAVNKVIKSYAKFSATPRYMTYN
dmRpt1	406	EKDFLEAVKKVIKSYAKFSATPRYMTYN
atRpt1	399	EKDFLDAVNKVIKGYQKFSATPKYMVYN
scRpt1	440	EKDFLKAVDKVISGYKKFSSTSRYMQYN

C

hsRpt6	380	QEDFEMAVAKVMQKDSEKNMSIKKLWK
mmRpt6	380	QEDFEMAVAKVMQKDSEKNMSIKKLWK
drRpt6	380	QEDFEMAVAKVMQKDSEKNMSIKKLWK
xlRpt6	388	QEDFEMAVAKVMQKDSEKNMSIKKLWK
dmRpt6	379	QEDFEMAVAKVMQKDSEKNMSIKKLWK
atRpt6	378	QEDFEMAVSKVMKKEGESNMSLQRLWK
scRpt6	379	QEDFELAVGKVMNKNQETAISVAKLFK

Figure S6

Figure S6 related to Figure 6. *A,* EM densities of the C-termini of Rpt6 (left) and Rpt1 (right). The Rpt6 C-termius is inserted between α2 and α3 and the Rpt1 C-terminus is inserted between α4 and α5. The EM density is depicted in gray. *B, C,* Boxshade alignments of the C-termini of Rpt1 (*B*) and Rpt6 (*C*) demonstrate high conservation of C-terminal amino acids.

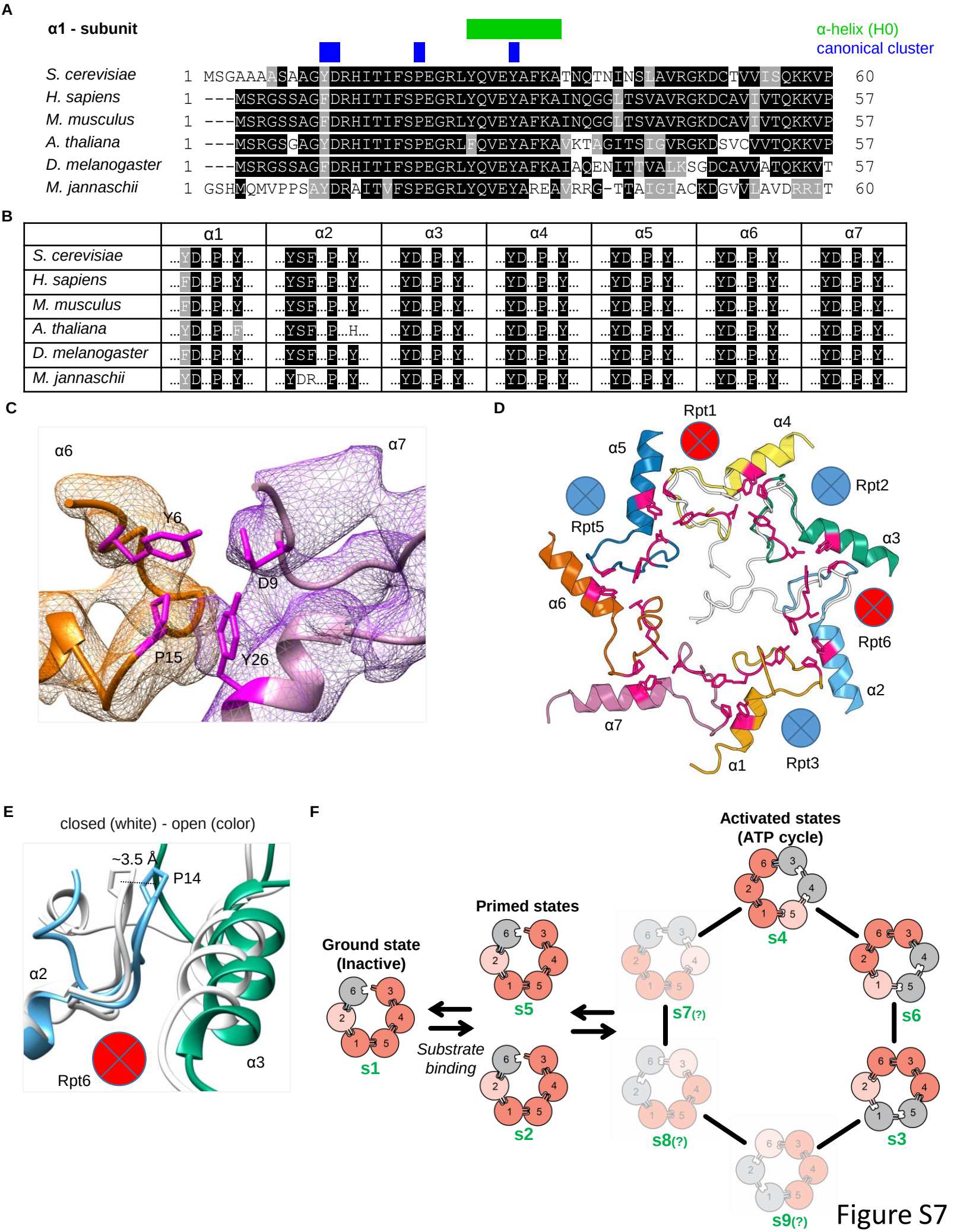
A
α1 - subunit
α-helix (H0)
canonical cluster
S. cerevisiae 1 MSGAAAASAAGYDRHITIFSPEGRLYQVEYAFKATNQTNINSLAVRGKDCTVVISQKKVP 60
H. sapiens 1 ---MSRGSSAGFDRHITIFSPEGRLYQVEYAFKAINQGGLTSVAVRGKDCAVIVTQKKVP 57
M. musculus 1 ---MSRGSSAGFDRHITIFSPEGRLYQVEYAFKAINQGGLTSVAVRGKDCAVIVTQKKVP 57
A. thaliana 1 ---MSRGSGAGYDRHITIFSPEGRLFQVEYAFKAVKTAGITSIGVRGKDSVCVVTQKKVP 57
D. melanogaster 1 ---MSRGSSAGFDRHITIFSPEGRLYQVEYAFKAIAQENITTVALKSGDCAVVATQKKVT 57
M. jannaschii 1 GSHMQMVPPSAYDRAITVFSPEGRLYQVEYAREAVRRG-TTAIGIACKDGVVLAVDRRIT 60
B
α1 α2 α3 α4 α5 α6 α7
S. cerevisiae ...YD...P...Y... ...YSF...P...Y... ...YD...P...Y... ...YD...P...Y... ...YD...P...Y... ...YD...P...Y... ...YD...P...Y...
H. sapiens ...FD...P...Y... ...YSF...P...Y... ...YD...P...Y... ...YD...P...Y... ...YD...P...Y... ...YD...P...Y... ...YD...P...Y...
M. musculus ...FD...P...Y... ...YSF...P...Y... ...YD...P...Y... ...YD...P...Y... ...YD...P...Y... ...YD...P...Y... ...YD...P...Y...
A. thaliana ...YD...P...F... ...YSF...P...H... ...YD...P...Y... ...YD...P...Y... ...YD...P...Y... ...YD...P...Y... ...YD...P...Y...
D. melanogaster ...FD...P...Y... ...YSF...P...Y... ...YD...P...Y... ...YD...P...Y... ...YD...P...Y... ...YD...P...Y... ...YD...P...Y...
M. jannaschii ...YD...P...Y... ...YDR...P...Y... ...YD...P...Y... ...YD...P...Y... ...YD...P...Y... ...YD...P...Y... ...YD...P...Y...
C
α6
α7
Y6
D9
P15
Y26
D
Rpt1
α4
α5
Rpt2
Rpt5
α3
α6
Rpt6
α2
α7
α1
Rpt3
E
closed (white) - open (color)
~3.5 Å
P14
α2
α3
Rpt6
F
Activated states (ATP cycle)
Primed states
Ground state (Inactive)
s1
s2
s3
s4
s5
s6
s7(?)
s8(?)
s9(?)
Substrate binding

Figure S7

Figure S7 related to Figure 7. *A*, Sequence alignment between *S. cerevisiae*, *H. sapiens*, *M. musculus*, *A. thaliana*, *D. melanogaster* and *M. jannaschii* of the first 60 amino acids of α1. The canonical clusters are marked in blue and the first α-helix in green. *B*, Sequence alignment of the canonical cluster amino acids of all seven α-subunits from *S. cerevisiae*, *H. sapiens*, *M. musculus*, *A. thaliana*, *D. melanogaster* and *M. jannaschii*. All canonical cluster amino acids but those from α2 of *M. jannaschii* are highly conserved, which explains the non-canoncial cluster formed between α1- α2. *C*, Example of YD-P-Y motif between α6 and α7 in the s5 state. The EM density is shown as mesh. *D*, The α subunit N-termini of α2, α3 and α4 undergo large movements between the closed and open gate conformations. Each N-terminus is depicted in a different color in the s5 state: α1 light orange, α2 light blue, α3 dark green, α4 yellow, α5 dark blue, α6 dark orange, α7 light pink. The localization of the N-terminal extensions of α2, α3 and α4 in the s2 state are visible in white. The structures of s2 and s5 were aligned onto the complete α chains of the CP. *E*, A proline movement of ~3.5 Å in α2 can be identified between all open and closed structures, here shown in states s5 (colored, light blue and dark green) and s2 (white). The C-terminus of Rpt6 inserts into the α subunit pocket between α2 and α3 in s3 (closed) and all open gate states, s4, s5 and s6. *F*, Model for ATP hydrolysis by 26S proteasome. In the absence of substrate, the proteasome is present in the ground state (s1), which represents the lowest energy conformation amongst the conformational states. When the proteasome is activated, most likely by substrate binding (Lu et al., 2015), it undergoes a conformational change from the ground state to a primed state (s2 or s5). The translocation of substrate may be triggered by ATP hydrolysis by one of the initiating ATPases coupled with ATP binding by Rpt6, leading the proteasome to an activated state (s3, s4 and s6). ATP hydrolysis can occur in either the lowermost engaged and most likely ATP-bound subunit, as was suggested for Yme1 (Puchades et al., 2017), or the highest engaged subunit (Martin et al., 2008), and continues around the ring. ATP hydrolysis causes a major conformational change in the neighboring subunits, leading to a new nucleotide-pocket configuration and to the next proteasome state of the hydrolysis cycle. Additional states may exist (s7, s8, s9). It is probable that the cycle continues until substrate translocation is completed. The cycle could include reversion to s2, s5, or s1.